Journal of
Materials Chemistry B

ROYAL SOCIETY
OF CHEMISTRY

REVIEW

View Article Online
View Journal | View Issue

Check for updates

Cite this: *J. Mater. Chem. B*, 2021, **9**, 3423

Applications of nanoscale metal–organic frameworks as imaging agents in biology and medicine

Fatma Demir Duman and Ross S. Forgan *

Nanoscale metal–organic frameworks (NMOFs) are an interesting and unique class of hybrid porous materials constructed by the self-assembly of metal ions/clusters with organic linkers. The high storage capacities, facile synthesis, easy surface functionalization, diverse compositions and excellent biocompatibilities of NMOFs have made them promising agents for theranostic applications. By combination of a large variety of metal ions and organic ligands, and incorporation of desired molecular functionalities including imaging modalities and therapeutic molecules, diverse MOF structures with versatile functionalities can be obtained and utilized in biomedical imaging and drug delivery. In recent years, NMOFs have attracted great interest as imaging agents in optical imaging (OI), magnetic resonance imaging (MRI), computed tomography (CT), positron emission tomography (PET) and photoacoustic imaging (PAI). Furthermore, the significant porosity of MOFs allows them to be loaded with multiple imaging agents and therapeutics simultaneously and applied for multimodal imaging and therapy as a single entity. In this review, which is intended as an introduction to the use of MOFs in biomedical imaging for a reader entering the subject, we summarize the up-to-date progress of NMOFs as bioimaging agents, giving (i) a broad perspective of the varying imaging techniques that MOFs can enable, (ii) the different routes to manufacturing functionalised MOF nanoparticles and hybrids, and (iii) the integration of imaging with differing therapeutic techniques. The current challenges and perspectives of NMOFs for their further clinical translation are also highlighted and discussed.

Received 19th February 2021,
Accepted 25th March 2021

DOI: 10.1039/d1tb00358e

rsc.li/materials-b

WestCHEM, School of Chemistry, University of Glasgow, University Avenue, Glasgow G12 8QQ, UK. E-mail: ross.forgan@glasgow.ac.uk

Fatma Demir Duman

Fatma Demir Duman is a postdoctoral research associate at the University of Glasgow. She was previously a postdoctoral researcher at University College London and Koc University. She received her PhD in Materials Science and Engineering from Koc University in 2017, her MSc in Bioengineering from Hacettepe University in 2012, and her BSc degrees in Molecular Biology and Genetics and Chemistry (double major) from Istanbul Technical University in 2010. Her research interest is focused on the design, synthesis and characterization of metal–organic frameworks, Cd-free quantum dots, and gold nanoparticles, and their conjugation with therapeutic and targeting ligands for cancer treatment and imaging.

Ross S. Forgan

Ross Forgan is Professor of Supramolecular and Materials Chemistry at the University of Glasgow. He obtained his PhD from the University of Edinburgh in 2008, and carried out postdoctoral research with Prof. Sir J. Fraser Stoddart (Northwestern University) and Prof. Lee Cronin (University of Glasgow). He has been the recipient of a Royal Society URF (2012), an ERC Starting Grant (2016), the Sessler Early Career Researcher Prize (2018) and the RSC Bob Hay Lectureship (2020). His research into the application of metal–organic frameworks in biomimetic catalysis and nanoscale drug delivery is underpinned by fundamental studies into the self-assembly processes of porous materials.

1. Introduction

Porous materials are increasingly becoming attractive in biomedical applications due to their excellent intrinsic properties, such as large tunable porosities and fine control of chemical composition.[1] Metal–organic frameworks (MOFs), which are also known as porous coordination polymers or porous coordination networks, are a class of porous hybrid solids that are formed by the self-assembly of metal ions or metal ion clusters and organic polydentate bridging linkers.[2,3] Owing to their structural and functional tunability, much effort has been made to develop MOFs, particularly nanoscale metal–organic frameworks (NMOFs), over the past two decades to apply them in many areas, including but not limited to gas separation, gas storage,[4,5] catalysis,[6,7] non-linear optics,[8,9] chemical sensing,[10–12] drug delivery[13–15] and imaging.[16–20]

NMOFs exhibit various characteristics that make them ideal materials for biomedical applications. Their highly porous structures and versatile functionality allow accommodation of high loadings of therapeutic and imaging agents and their controlled release, as well as protection against enzymatic degradation and self-quenching in living systems.[21–24] Compared with conventional nanomaterials such as inorganic zeolites, mesoporous silica, quantum dots, metal nanoparticles, and organic nanocarriers of lipids or polymers, NMOFs typically possess a larger cargo loading capacity, good biocompatibility and ease of functionalisation.[25] In the longer term, NMOFs are also intrinsically biodegradable as a result of their relatively labile metal–ligand bonds.[26] The effectively infinite combination of metal clusters and organic linkers contributes to their compositional and structural tunability and allows the production of NMOFs with various pore sizes ranging from micropores to macropores, rigid or flexible skeletons, and diverse surface chemistries.[27] Furthermore, their mild synthetic conditions enable the design of numerous NMOFs and incorporation of a large variety of molecular functionalities on their inner and outer surfaces, including imaging modalities, therapeutics and targeting ligands.

Since Lin and co-workers first reported the design of NMOFs as potential multimodal contrast enhancing agents for biomedical imaging in 2006,[28] an increasing number of studies have used them as imaging agents for optical imaging (OI), magnetic resonance imaging (MRI), computed tomography (CT), positron emission tomography (PET) and photoacoustic imaging (PAI).[18,28–37] NMOFs offer a potential new class of imaging agents combining the characteristics of both inorganic and organic nanomaterials; the ease of construction of structures with metal ions/clusters or linkers with imaging abilities, or their doping with imaging molecules, makes them highly promising candidates. In comparison to existing imaging agents, NMOFs can offer high loading capacities for cargo molecules, high protection against enzymatic degradation, minimal release in the blood, and efficient delivery to targeted tissues, in contrast to the short blood circulation times and non-specific biodistributions often characteristic of conventional imaging agents.[38] For example, NMOF-based MRI contrast agents have shown enhanced relaxivities compared to commercially available Gd contrast agents[39] and even other Gd nanoparticulate systems,[40,41] while an archetypal Hf MOF showed superior contrast for computed tomographic imaging compared to an I-based agent, even at a lower dose, that could be promising in decreasing the radiation dose to which the patients must be exposed.[42] Moreover, NMOFs can be employed as multimodal imaging agents by the combination of multiple imaging functionalities in a single entity, and as image-guided therapy agents by achieving simultaneous imaging and therapy.[43–45]

There are four main approaches for the construction of MOFs containing imaging agents (i) encapsulation of the agents within the pores of MOFs during the synthesis, (ii) their incorporation as intrinsic structural components of MOFs, (iii) immersion of already synthesized MOFs in a solution of imaging agents and so loading them inside the pores by size effect, ion-exchange or post-synthetic modification, collectively known as the post-insertion method, and (iv) attachment of imaging agents by covalent conjugation, or electrostatic or hydrophobic interactions, to the surface of MOFs as shown in Scheme 1.[46–49]

In this review, we will highlight the preparation and applications of NMOFs as imaging and theranostic agents in the biomedical field. Compared to other excellent reviews related to the applications of MOFs in biomedicine,[27,50–52] imaging and sensing,[38,48,53,54] or theranostics,[55,56] this review will solely focus on and discuss the bioimaging applications of NMOFs, exemplifying the different strategies to facilitate mono- and multimodal imaging with select examples, and offering insight into the combination of imaging with other biological applications. This review is not intended to be a comprehensive overview of the field, but an introduction to the varying biomedical imaging techniques that MOFs can be

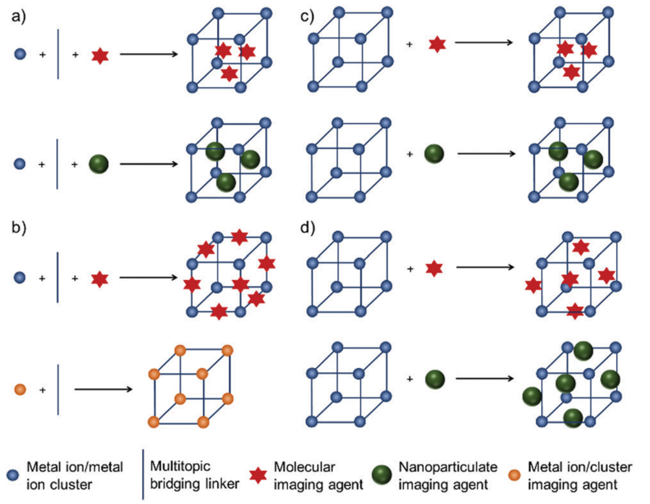

Scheme 1 Main approaches for the construction of MOFs with imaging capabilities. (a) The *in situ* encapsulation of imaging agents during MOF synthesis. (b) Their integration as intrinsic components of the MOF, either as a linker or metal ion or metal cluster. (c) Postsynthetic loading of imaging agents into the porosity of the MOF. (d) Postsynthetic functionalisation of the MOF particle surface with imaging units.

applied to and a discussion of the varying methodologies to engender MOFs with imaging functionality.

2. MOFs as monomodal imaging agents

2.1. Optical imaging

Optical imaging (OI) is an imaging modality that uses light illumination at visible or near-infrared (NIR) wavelengths, which can be detected by optical cameras.[57] OI provides real-time visualization of organs, tissues, and cells and monitors the progression of any morphological and biochemical changes non-invasively, allowing intraoperative image-guided surgery. The technique employs neither ionizing radiation, as in computed tomography, nor radioactive compounds, as in positron emission tomography, and it is a rapid and suitable imaging mode for high-throughput screening for both *in vitro* and *in vivo* imaging with non-invasion and high signal sensitivity.[17] The basis of the technique relies on the absorption of the externally applied photon energy of a certain wavelength by fluorophores, and then its emission as a new photon with energy in the longer wavelengths. However, OI has limitations in terms of quantifying fluorescence intensity in living organisms accurately due to auto-fluorescence, intrinsic tissue signal attenuation, and the shallow tissue penetration of light. Therefore, many fluorescent materials have been investigated to obtain strong optical imaging agents that can offer deep tissue and intracellular imaging.[58]

Luminescent MOFs have been utilized as effective optical imaging agents in the last two decades due to their attractive properties such as high payloads, tailorable surface chemistry that provides improved pharmacokinetics, and tunable sizes and structures.[38] Various MOF structures with luminescent properties for optical biomedical imaging have been developed by combining MOFs with fluorescent dyes, photosensitizers or fluorescent drugs,[13,18,29,34,59–72] metal ions/clusters (particularly lanthanides),[23,73] or luminescent nanoparticles such as persistent luminescent nanoparticles (PLNPs),[74,75] upconversion nanoparticles (UCNPs)[76–78] or quantum dots (QDs).[79]

2.1.1. Combination with fluorescent dyes/photosensitizers/fluorescent drugs. Combining MOFs with fluorescent dyes, photosensitizers, or fluorescent drugs – particularly anticancer drugs – by using them as a linker or a cargo molecule is a very advantageous way to obtain various MOFs that emit in different ranges of the optical spectrum. This strategy is also very effective to prevent aggregation-induced quenching and achieve consistent luminescence features under harsh conditions by the confinement effect within the pores of MOFs, hence improving the photoluminescence performances and efficiencies of the fluorescent species.[46] By using these approaches, various fluorescent dyes, photosensitizers or fluorescent drugs have been incorporated into different types of MOFs for the detection of diseases with high sensitivity, or determination of cellular uptake efficiency of synthesized MOF systems.[18,29,59–63,69,71,72,80]

Fluorescent dyes. Liu *et al.* have reported the synthesis of phosphorescent MOFs using a phosphorescent ruthenium complex, [Ru(2,2′-bipyridyl-5,5′-dicarboxylic acid)(2,2′-bipyridine)$_2$], as bridging ligand, and Zr(IV) or Zn(II) connecting points, achieving a dye loading of 57.4% and 78.7%, respectively.[17] Then, the synthesized nanoparticles were further stabilized with a silica coating, functionalized with poly(ethylene glycol) (PEG) and an anisamide targeting molecule which provided a cancer specific optical imaging of H460 lung cancer cells *in vitro*. Furthermore, the results showed that zirconium MOFs exhibited higher stability in aqueous conditions compared to zinc MOFs. On the other hand, Ryu *et al.* size-selectively encapsulated resorufin and rhodamine-6G within nanocrystalline metal–organic frameworks (NMOFs, Fig. 1a), MOF-801, $[Zr_6O_4(OH)_4(\text{fumarate})_6]_n$, also known as Zr-fum, in which the linker is fumaric acid, and UiO-67, $[Zr_6O_4(OH)_4(BPDC)_6]_n$ (BPDC = 4,4′-biphenyldicarboxylate, UiO: Universitetet i Oslo), during their crystal growth and obtained resorufin-in-nMOF-801 (Rs$\subset$nMOF-801) and rhodamine-6G-in-nUiO-67 (R6G$\subset$nUiO-67). The Zr-MOF nanoparticles showed exceptional stabilities in biomedical environment, and enhanced photoluminescence properties, such that they could preserve the fluorescence even after 9 days.[18] The resulting particles were successfully utilized for reliable and reproducible fluorescence imaging of FL83B human hepatocyte cells and HepG2 human hepatocellular carcinoma cells after being functionalized by galactosylation, to improve the biocompatibility and cellular uptake of MOFs through the high attachment affinity of galactose residues on the nanoparticles to the asialoglycoprotein receptors in the plasma membranes of liver cells (Fig. 1b–e).

In another study, Gao *et al.* showed encapsulation of rhodamine b (RhB) within a hierarchical-pore metal–organic framework (H-MOF), using a one-step approach that was achieved by assembling MIL-53(Al)-NH$_2$, constructed from [AlO$_6$] octahedral chains connected by 2-aminobenzene-1,4-dicarboxylate (BDC-NH$_2$) linkers, with formula $[Al(OH)(BDC\text{-}NH_2)]_n$ and where MIL stands for Materials of Institute Lavoisier, in an aqueous solution of RhB, which serves as a fluorescent imaging agent.[29] The obtained red fluorescence emitting H-MOFs were employed for *in vitro* imaging of murine gastric cancer 803 (MGC-803) cells and human airway smooth muscle cell (HASMC), and allowed *in vivo* imaging of athymic nude mice with good stability, biocompatibility and high imaging efficiency, avoiding the interference of autofluorescence. Furthermore, the as-synthesized fluorescent HMOFs were also successfully utilized as a nanocarrier by simultaneously loading the macromolecular drug tetracycline hydrochloride (TCH) and small molecule anticancer drug 5-fluorouracil (5-FU) with high loading efficiency, and delivery into cells. Mao and co-workers reported the fabrication of MOF-based fluorescent probes self-assembled from Zn(II) and imidazole-2-carboxyaldehyde (ICA), namely nanoscale ZIF-90 (formula $[Zn(ICA)_2]_n$, where ZIF stands for zeolitic imidazolate framework), to target sub-cellular mitochondria and visualize mitochondrial adenosine triphosphate (ATP) in live cells.[81] Rhodamine (RhB) was encapsulated into ZIF-90 during synthesis, which resulted in its quenching due to the self-quenching effect of RhB (Fig. 2a). In the presence of ATP, the competitive coordination between

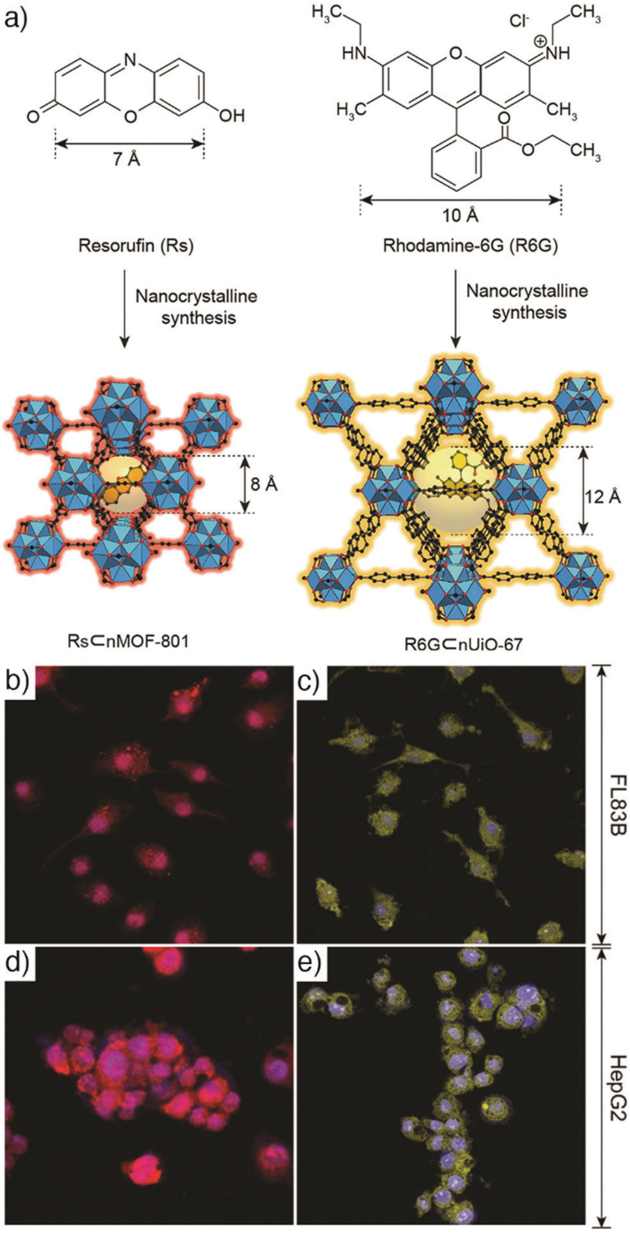

Fig. 1 (a) Scheme for the encapsulation of resorufin and rhodamine-6G within NMOFs to produce Rs⊂nMOF-801 and R6G⊂nUiO-67, respectively. Confocal laser scanning microscopic images of (b) and (c) FL83B cells, and (d) and (e) HepG2 cells, after treatment with (b) and (d) galactosylated Rs⊂nMOF-801, and (c) and (e) galactosylated R6G⊂nUiO-67. Reproduced with permission.[18] Copyright (2017) American Chemical Society.

ATP and the metal node of ZIF-90 led to the decomposition of RhB/ZIF-90 complex and consequently release and fluorescence recovery of RhB, and thus mitochondrial ATP imaging in living cells as shown in Fig. 2b–e.

MOFs were also successfully loaded with 1,3,5,7-tetramethyl-4,4-difluoro-8-bromomethyl-4-bora-3*a*,4*a*-diaza-*s*-indacene (Br-BODIPY) fluorescent dye by postsynthetic modification (PSM) of iron-carboxylate MIL-101(Fe) (trimeric iron(III) octahedral clusters connected with benzene-1,4-dicarboxylate (BDC) linkers of formula $[Fe_3O(BDC)_3(H_2O)_2X]_n$, where X is a monocounterion typically OH^- or Cl^-) and used as optical imaging contrast agents for HT-29 human colon adenocarcinoma cells.[59] To increase the stability of the particles and decrease cargo release, the nanosized MIL-101(Fe) particles were further functionalized by a silica coating and conjugated with the cisplatin prodrug (ethoxysuccinato-cisplatin, ESCP) for anticancer therapy. The cytotoxicity studies showed efficient cancer cell killing with the ESCP loaded nanoparticles, but slightly less cytotoxicity than free cisplatin. The functionalization of nanoparticles with a cancer targeting peptide, c(RGDfK), which has high binding affinity toward $\alpha_v\beta_3$ integrin overexpressed on cancer cells, slightly improved the cytotoxic effect of the nanoparticles providing similar IC_{50} (the half maximal inhibitory concentration) to that of free cisplatin. Such materials that combine imaging and drug delivery are often termed theranostics, for which MOFs are highly suited.[55,56]

Similarly, Wuttke *et al.* reported the encapsulation of fluorescein dye in lipid-coated MOF nanoparticles and their successful cellular uptake.[60] In the study, the mesoporous iron(III) carboxylate MIL-100(Fe), which is constructed from octahedral trimers connected by benzene-1,3,5-tricarboxylate (BTC) to give formula $[Fe_3O(BTC)_2(H_2O)_2X]_n$ with large pore (diameter 2.4–2.9 nm) and window sizes (0.6–0.9 nm), and the mesoporous chromium(III) analogue MIL-101(Cr) with large pore (diameter 2.9–3.4 nm) and window sizes (1.2–1.7 nm), were loaded with fluorescein dye. The dye-loaded MOF nanoparticles were subsequently encapsulated by the formation of a bilayer of lipid DOPC (1,2-dioleoyl-*sn-glycero*-3-phosphocholine) through a controlled solvent-exchange deposition of the lipid molecules onto the MOF surface. The MOF@lipid nanoparticles synergistically combined the properties of liposomes and porous particles, storing the dye molecules inside the MOF pores while the lipid coating prevented the premature release of the dye and improved the colloidal stability of the nanoparticles. *In vitro* fluorescence microscopy studies showed high accumulation of the fluorescein-loaded nanoparticles with strong emission in T24 human bladder carcinoma cells.

The well-known low-toxic luminescent organic dye calcein (cal) has often been employed as a model drug in order to determine the cell internalization and drug delivery potential of MOF nanoparticles.[69,82–84] Calcein is a hydrophilic fluorophore that is unable to cross cell membranes in significant quantities; rather the fluorescent molecule needs a drug delivery system (DDS) to facilitate its transport. In addition, calcein has a self-quenching nature at high concentrations that makes the vesicles carrying high local concentrations of calcein undetectable by fluorescent microscopy. However, upon its release from the carriers and dilution in the cytoplasmic environment, the green fluorescence of calcein can be detected by fluorescence-based techniques.[85] Calcein was postsynthetically incorporated into Zr-based MOFs of the UiO topology by Orellana-Tavra *et al.* to study the endocytosis mechanism of Zr-MOFs through linker functionalization (Fig. 3a).[64] In the study, UiO-66 topology MOFs with general formula $[Zr_6O_4(OH)_4(BDC)_6]_n$ were prepared with different particle sizes and different surface chemistries by substituting the original BDC linker with functionalized or

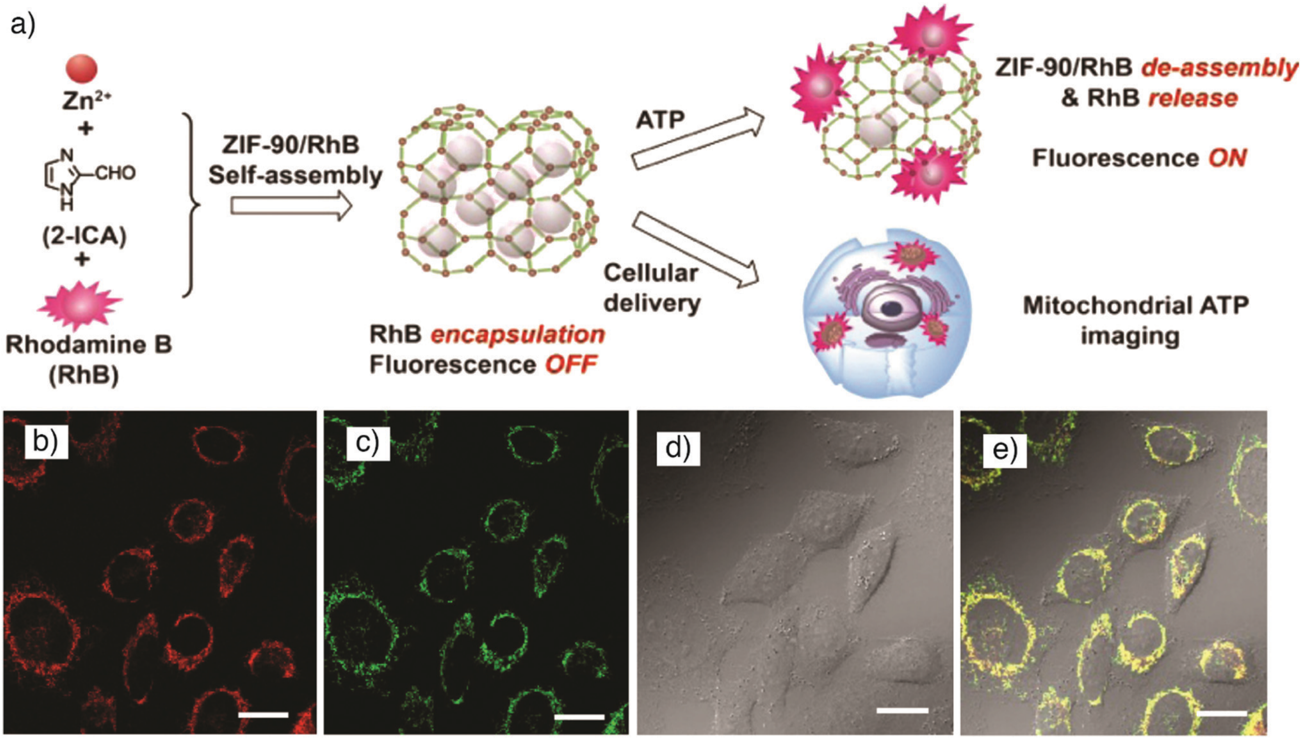

Fig. 2 (a) Schematic illustration for the synthesis of RhB/ZIF-90 and host–guest chemistry for fluorescent ATP sensing and mitochondrial ATP imaging in living cells. Confocal laser scanning microscopy images of HeLa cells incubated with (b) RhB/ZIF-90 nanocrystals for 2 h (λ_{ex} = 559 nm; λ_{em} = 570–670 nm), and (c) rhodamine 123 for 15 min (λ_{ex} = 488 nm; λ_{em} = 500–545 nm). (d) Bright-field image of HeLa cells, and (e) overlay of images (b)–(d). Scale bars represent 20 μm. Reproduced with permission.[81] Copyright (2017) American Chemical Society.

extended linkers, and subsequently loaded with calcein. Fig. 3b schematizes the linkers (L1–L6) used in the study to build the Zr-based MOFs termed as Zr-L1 to Zr-L6, where L1 is BDC; L2–L4 are BDC functionalized with –Br, $-NO_2$, and $-NH_2$, respectively; L5 and L6 are extended linkers naphthalene-2,6-dicarboxylic acid (NDC) and BPDC, respectively. While the particle size does not significantly affect the cellular uptake mechanism in HeLa cells, visualised by intracellular calcein, control of surface chemistry through linker functionalization has a great influence. After 2 h incubation, a high degree of cal@Zr-L2, cal@Zr-L3 and cal@Zr-L4 were localized in cells as seen in Fig. 3c. The endocytosis mechanism can also be probed by the use of selected pharmacological endocytosis inhibitors, which demonstrated minimal particle size effects on uptake of cal@Zr-L1 (Fig. 3d), but also that cal@Zr-L1 (unfunctionalized) and cal@Zr-L3 ($-NO_2$ functionalized) are taken up mostly through clathrin-mediated endocytosis, while cal@Zr-L5 and cal@Zr-L6 are taken up by the caveolae-mediated route, and so may avoid lysosomal degradation, although their total uptake is less than the others (Fig. 3e).

In another study, Haddad *et al.* utilized calcein to track the mitochondria targeting efficiencies of UiO-66 nanoparticles loaded with the anticancer drug dichloroacetate (DCA) and functionalized with a triphenylphosphonium (TPP) targeting unit,[69] which is a lipophilic cation that accumulates in mitochondria as a consequence of the mitochondrial membrane potential in living cells.[65] They reported that MCF-7 human breast cancer cells treated with the targeted MOF system, cal-TPP@(DCA_5-UiO-66) demonstrated changes in mitochondrial morphology from elongated and reticular networks (untreated cells, Fig. 4, left) to short, balloon-shaped, fragmented mitochondria (Fig. 4, right) as a result of the DCA toxicity, as observed by structured illumination microscopy. This effect was less active with non-targeted cal@(DCA_5-UiO-66) which showed still partially stringy and reticular morphology, as shown by the white arrows in Fig. 4 (centre). The presence of the MOF in the cells could be ascertained by the green fluorescence of the calcein.

Photosensitisers. The integration of photosensitizers such as porphyrins, chlorins or indocyanine green (ICG) into MOFs is another approach to obtain MOFs with optical imaging capability. This class of MOFs, named photosensitizer-based MOFs, can act as multifunctional nanoplatforms combining both photothermal imaging and photodynamic therapy (PDT) characteristics. Particularly, porphyrins and their analogues have been widely investigated due to their unique optoelectronic properties and versatility.[71,72,80] Furthermore, the integration of porphyrins into MOF structures prevents their easy aggregation and quenching – a consequence of their large hydrophobic planar structures – and retains their optoelectronic properties.[45]

To obtain porphyrin-based MOFs, two different approaches have primarily been conducted. In the first approach, which results in porphyrin@MOFs, porphyrins are integrated within MOFs as guest molecules through encapsulation into the pores or adsorption on the surface *via* non-covalent interactions such

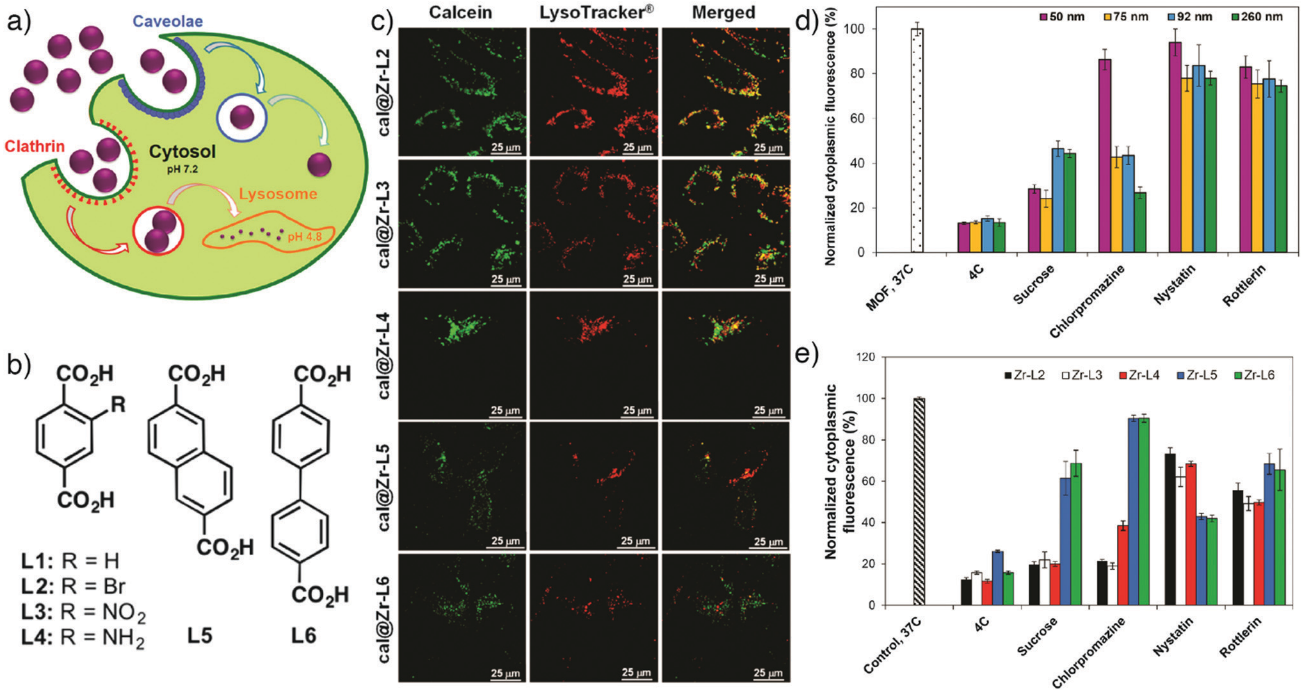

Fig. 3 (a) Schematic illustration of different endocytosis mechanisms of Zr-based MOFs. (b) Chemical structures of linkers used to synthesize the Zr-MOFs. (c) Confocal microscopy images of HeLa cells treated with calcein incorporated Zr-based MOFs for 2 h (green fluorescence indicates calcein, red shows lysosome marker LysoTracker-Deep red). Effects of pharmacological endocytosis inhibitors on the uptake of (d) Zr-L1 with different particles sizes, and (e) linker functionalized Zr-based MOFs, as measured by flow cytometry tracking calcein fluorescence. Reproduced with permission.[64] Copyright (2017) American Chemical Society.

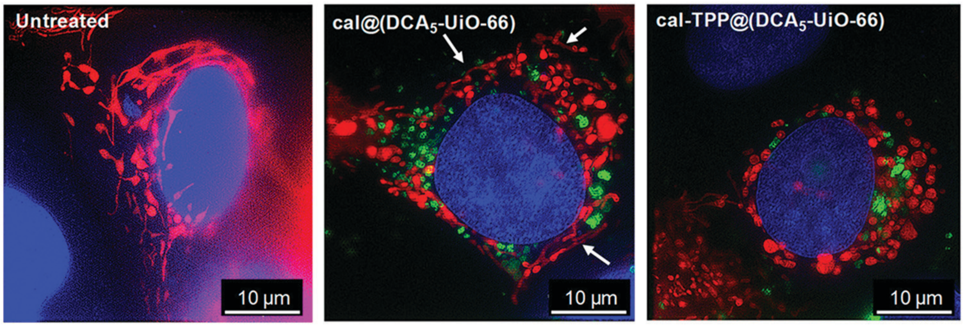

Fig. 4 Structured illumination microscopy images of untreated (left), cal@(DCA_5-UiO-66) treated (centre), and cal-TPP@(DCA_5-UiO-66) (right) treated MCF-7 cells 8 h after incubation. Red fluorescence indicates mitochondria stained with a red fluorescent protein (RFP), blue corresponds to nuclei stained with DRAQ-5™, and green shows MOFs loaded with calcein. White arrows indicate stringy mitochondria. Reproduced with permission.[69] Copyright (2020) American Chemical Society.

as van der Waals forces, π–π stacking, or electrostatic interactions, or conjugation through covalent or coordinative bonds.[86,87] The second approach uses porphyrins as organic linkers due to their macromolecular heterocyclic structures which can easily be functionalised with groups capable of coordination with metal ions or clusters. This class of MOFs is typically characterized by high porosities that allow accommodation of multiple functional units. Mostly, carboxylate-functionalised porphyrins such as 5,10,15,20-tetrakis(4-carboxyphenyl)porphyrin (TCPP) are used as linkers and coordinated with metals to form porphyrinic MOFs. The divalent metal ions such as Zn, Cu, Co and Cd typically coordinate to TCPP to produce 2D MOFs, while tri-and tetravalent Zr, Fe, Hf or Mn metal ions usually form porphyrinic MOFs with 3D structures.[87–90] For example, Liu *et al.* have reported the construction of biocompatible nanoscale zirconium–porphyrin metal–organic framework (NPMOF)-based imaging-guided therapy systems by using a microemulsion strategy and tuning the reaction conditions carefully.[71] The NPMOFs were synthesized *via* a microemulsion template and the auxiliary ligand method using $ZrCl_4$ metal precursor and 5,10,15,20-tetrakis (4-carboxyl)-21*H*,23*H*-porphine (TCPP) ligand as well as benzoic acid as the auxiliary ligand, PEG-6000 as capping agent, and cetyltrimethylammonium bromide (CTAB) as surfactant, in DMF at 120 °C for 24 h that resulted in spindle-like particles. The further incubation of the reaction solution under these conditions caused the formation of bulk zirconium–porphyrin metal–organic frameworks with a rod-like shape after 40 h, maintaining the crystal structure of NPMOFs. The obtained MOFs exhibited efficient fluorescent imaging and PDT by achieving high porphyrin loading (59.8%), and high chemotherapy efficacy in tumour tissues through high doxorubicin loading (109% w/w).

Porphyrinic MOFs can also be combined with other functional nanoparticles due to their porosity, to form multifunctional compositions. For example, Zeng *et al.* showed the fabrication of core–shell gold nanorod@porphyrinic MOFs as multifunctional theranostic nanoparticles for combined photodynamic/photothermal/chemotherapy of tumour.[80] The core–shell nanocomposites (Fig. 5a and b) were prepared by the growth of a porphyrinic Zr-MOF, composed of 6-connected Zr_6 clusters and TCPP with the formula $[Zr_6O_4(OH)_4(H_2O)_6(OH)_6(TCPP)_{1.5}]_n$, on the surface of functionalized gold nanorods (AuNRs), which acted as seed crystal in the synthesis, and loaded with camptothecin (CPT) anticancer drug for chemotherapy of tumour. The as-synthesized AuNR@MOFs@CPT demonstrated high accumulation in the tumour tissues, exhibiting strong fluorescence intensity arising from porphyrinic MOFs (Fig. 5c–g), and high photothermal activity of AuNRs, evident in the photothermal images of 4T1 tumour-bearing mice irradiated with 808 nm laser after 24 h intravenous injection of AuNR@MOFs@CPT (Fig. 5h and i), therefore achieving high synergistic efficiency of photodynamic, photothermal and chemo-therapies in the tumour.

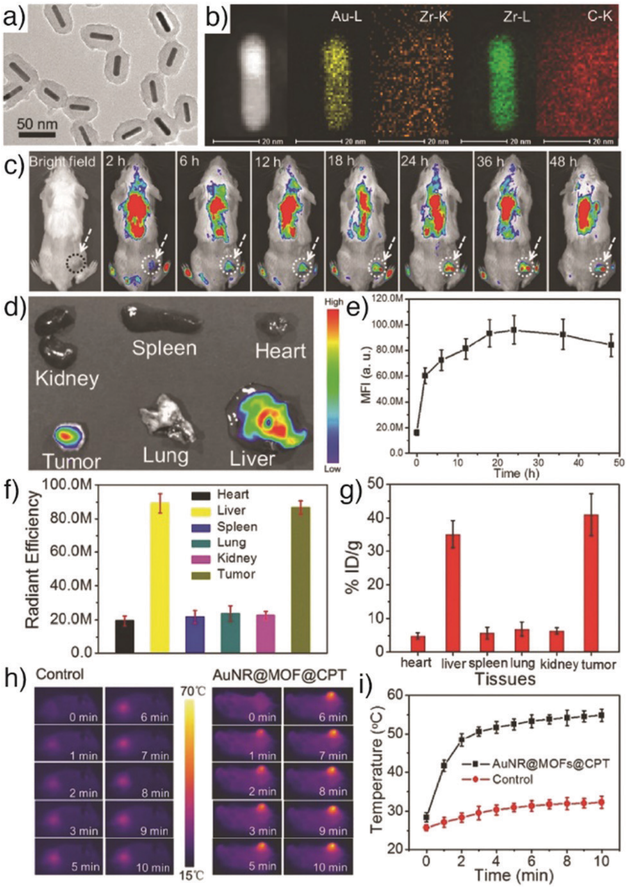

Fig. 5 (a) TEM image of AuNR@MOFs showing the core–shell structure. (b) EDX elemental mapping of AuNR@MOFs. (c) Fluorescence images of a 4T1 tumour-bearing mouse at different time points after being injected with AuNR@MOFs@CPT. (d) *Ex vivo* fluorescence images of major organs and tumour at 24 h post-injection. (e) Time-dependent quantitative fluorescence intensity detected in tumour tissues. (f) Quantitative fluorescence intensity of major organs and tumour. (g) Concentration of gold in major organs and tumour measured by ICP-AES at 24 h post-injection. Irradiation time-dependent (h) *in vivo* thermal images and (i) temperature change curve of mice after being injected with PBS (control) and AuNR@MOFs@CPT under 808 nm laser irradiation. Reproduced with permission.[80] Copyright (2017) Wiley-VCH Verlag GmbH & Co. KGaA, Weinheim.

Ju and co-workers showed a different approach for fluorescence cell imaging using photosensitizers.[91] The amino-functionalized iron(III) carboxylate MOF, MIL-101(Fe)-NH_2 (a derivative of MIL-101(Fe) where the linker is BDC-NH_2), was loaded with camptothecin through non-covalent encapsulation, and subsequently functionalized with a folic acid cancer targeting moiety and chlorin e6 (Ce6)-labelled cathepsin B (CaB) substrate peptide to act as the recognition unit, photosensitizer, and signal switch. CaB is a lysosomal cysteine endopeptidase overexpressed in many types of cancer cells. To target CaB and monitor the targeting effect, a CaB-substrate was conjugated with a Ce6 photosensitizer, which resulted in quenching of Ce6 due to the electron transfer from the excited Ce6 to MOFs. Upon incubation of the nanoparticles in cancer cells, Ce6 was released from the CaB-substrate by the cleavage of the substrate *via* intracellular CaB, and its fluorescence intensity was recovered, providing fluorescence imaging of the cancer cells. In addition to CaB-activatable fluorescence imaging, the nanoparticles demonstrated a significant tumour killing effect by synergistic chemo-photodynamic therapy, which overcomes the multidrug resistance of cancer cells and the low efficiency of PDT due to hypoxia in cancer cells.

To obtain luminescent MOFs using fluorescent salts, Singh *et al.* synthesized five different fluorescent nanosized salts/NMOFs by reacting 1,5-naphthalenedisulfonic acid (NDS) and $Cu(NO_3)_2{\cdot}3H_2O$ with a variety of N-heterocyclic ditopic pyridyl based highly fluorescent sensitizers, *i.e.*, 9,10-bis((*E*)-2-(pyridin-4-yl)vinyl)anthracene (B4PVA), 9,10-bis((*E*)-2-(pyridin-3-yl)vinyl)anthracene (B3PVA), and 3,3′-(peroxybis(methylene))dipyridine (3PBP) by a diffusion method.[70] The resulting fluorescent nanoparticles (FNP) – $[NDS^{2-}{\cdot}B4PVA^{2+}{\cdot}S]$ (FNP 1a), $[NDS^{2-}{\cdot}3PBP^{2+}{\cdot}MeOH{\cdot}H_2O]$ (FNP 1b), [Cu·NDS·B4PVA] (FNP 1c), [Cu·NDS·B3PVA] (FNP 1d), and [Cu·NDS·3PBP] (FNP 1e) – were of sizes below 100 nm, exhibited supramolecular architectures of the salts/MOFs, and showed high fluorescence arising from pyridylvinyl in the MOF scaffold. The synthesized particles had low cytotoxicity and a clear strong fluorescence signal in the green channel within HeLa and MCF-7 cell lines at the concentration of 10 μg mL^{-1} (Fig. 6).

Drugs. Doxorubicin (DOX) is an important chemotherapy agent which inhibits DNA replication by intercalating into the DNA double helix and inducing free radical generation.[92,93]

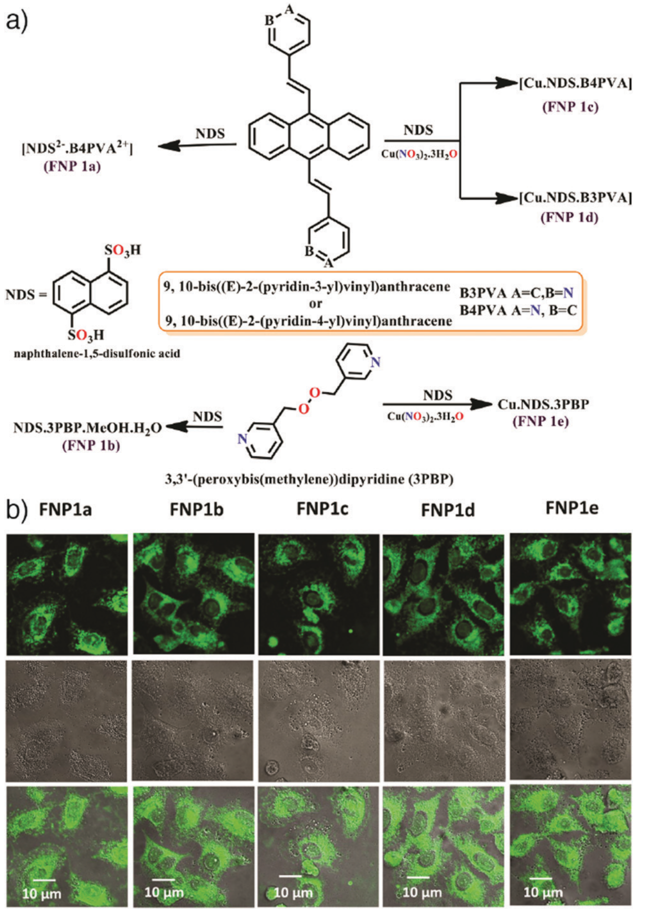

Fig. 6 (a) Schematic illustration for the synthesis of five different fluorescent nanosized salts/NMOFs. (b) Confocal laser scanning microscopy images of HeLa cells treated with FNP 1a–1e with a concentration of 10 µg mL^{-1} for 1 h. Reproduced with permission.[70] Copyright (2018) American Chemical Society.

However, direct administration of the drug causes undesired side effects by affecting both malignant and non-malignant cells in the body. Therefore, the delivery of the drug has been mostly studied with nanocarriers, and DOX was the first drug to receive clinical approval as a nanoformulation, delivered by a PEGylated liposome.[94] In addition to the apoptotic effects, its highly fluorescent nature makes the drug a popular agent to allow nanocarriers to be used as imaging agents as well as therapeutics.[95,96] Due to the high drug loading capacity, DOX has been widely studied with MOF structures for both therapy and imaging of tumour tissues.[13,34,66–68] For example, Li *et al.* reported the application of DOX loaded UiO-68-type NMOFs (isoreticular extensions of UiO-66 with terphenyl-based ligands) with a tumour-targeting agent (folic acid, FA) as targeted therapy and imaging system for hepatoma (HepG2) both *in vitro* and *in vivo*.[66] The NMOFs were prepared as shown in Fig. 7, firstly by the synthesis of Mi-UiO-68 from the maleimide-modified terphenyl ligand, H_2L, and $ZrCl_4$ in a DMF solution at 120 °C, followed by their DOX loading to produce DOX@Mi-UiO-68, and finally their decoration with thiolated FA units *via* a thiol–maleimide Michael-type addition. The obtained DOX@UiO-68-FA exhibited higher antitumour efficacy compared to free DOX and FA-undecorated DOX@Mi-UiO-68, which was confirmed by cell imaging *via* DOX, 3-(4,5-dimethylthiazol-2-yl)-2,5-diphenyltetrazolium bromide (MTT) cell viability assay, and *in vivo* studies using a HepG2 subcutaneous xenograft murine model (Fig. 7).

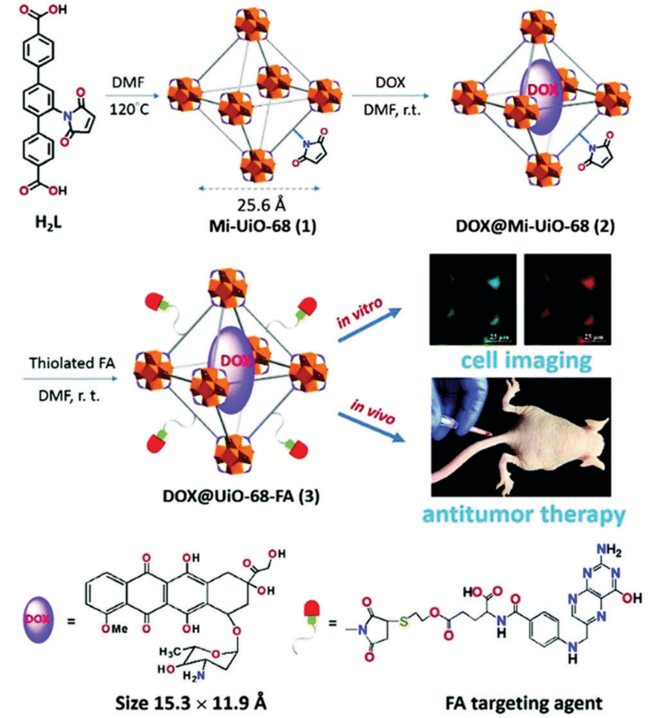

Fig. 7 Schematic of the synthesis and application of DOX loaded and FA conjugated Mi-UiO-68 MOFs for targeted cell imaging and antitumour therapy. Reproduced with permission.[66] Copyright (2016) The Royal Society of Chemistry.

2.1.2. Lanthanide MOFs. Materials based on lanthanide fluorescence have attracted great attention due to their sharp and stable emission, large and effective Stokes shifts, long-lived fluorescence lifetimes, and improved spectral and time-resolved signal discrimination from background autofluorescence.[97] Most of the luminescent lanthanide cations are notably resistant to photobleaching in a broad range of environmental conditions compared to organic fluorophores, which ensures their repeated usage over long periods of time.[98,99] In addition, the luminescence of lanthanide ions can be dramatically enhanced using a photonic converter, such as an organic chromophore, through the "antenna effect".[100] The molecules acting as antennae must be closely located to the lanthanide to enable sensitization. Lanthanide MOFs (Ln-MOFs) such as Eu-MOFs, Tb-MOFs and Yb-MOFs are therefore excellent luminescent particles, closely connecting lanthanide metals to π-conjugated organic linkers, which act as antennae, and typically exhibiting good photostability and characteristic fluorescence emission.[23,101,102] For example, Abazari *et al.* have reported the synthesis of a luminescent amine-functionalized Eu-MOF, Eu:TMU-62-NH_2 (TMU stands for Tarbiat Modares University) with 9-coordinate Eu(III) centres connected by BDC-NH_2 into a MOF with formula $[Eu_2(BDC\text{-}NH_2)_3(DMF)_4]_n$, which was conjugated with folic acid (FA) for targeted delivery of the anticancer drug 5-fluorouracil (5-FU) to MCF-7 breast cancer cells with concomitant *in vitro* fluorescence cell imaging.[103] Microscopy images exhibited higher cellular uptake of the folic acid conjugated structures compared to the unconjugated ones confirming the targeting effect of FA, and also red fluorescence emission arising from Eu:TMU-62-NH_2 which can be used for imaging. 5-FU-loaded FA@Eu:TMU-62-NH_2 showed excellent release of 5-FU in an acidic environment, implying pH-controlled release characteristics of this material, which is very suitable to target solid tumours. In addition, the nanoparticles dramatically decreased the cell viability of MCF-7 cells in a time- and dose-dependent manner, and increased reactive oxygen species (ROS) generation and apoptosis compared to free 5-FU.

On the other hand, many lanthanide cations emit in the NIR window of the optical spectrum, which allows deeper tissue imaging than visible light. This is due to the higher tissue penetration of NIR light as a result of lower scattering and absorbing effects of tissues at longer wavelengths, which also provides lower background fluorescence, less signal loss, and thus a higher signal to background ratio.[23,104] For example, Gallis *et al.* have reported the construction of a novel multifunctional MOF materials platform based on rare-earth (Eu, Nd, Yb, Y, and Tb) hexanuclear single metal clusters, as well as tuned compositions of Nd/Yb ($Nd_{0.67}/Yb_{0.33}$ and $Nd_{0.46}/Yb_{0.54}$) coordinated by 2,5-dioxybenzene-1,4-dicarboxylate (DOBDC) in the UiO-66 topology with general formula $[Ln_6(OH)_8(DOBDC)_5(DOBDC\text{-}H_2)(H_2O)_6]_n$.[73] The synthesized MOF materials exhibited both porosity and tunable emission properties over a wide range, from deep red into the second NIR window (~614–1350 nm) as a function of the metal identity. In addition to this, they met fundamental prerequisites for relevance to biological applications by demonstrating minimal *in vitro* cytotoxicity and maintaining crystallinity under relevant physiological conditions such as water and phosphate-buffered saline (PBS). The group used EuDOBDC nanoparticles as a proof-of-concept system in this series for *in vitro* imaging of RAW 264.7 mouse macrophage and HeLa human cervical cancer cells. Their results presented an efficient discrimination between the Eu emission and cell autofluorescence and a long-term conservation of the intrinsic emission in live cells, proving the application of the materials as long-term imaging agents.

Similarly, Foucault-Collet *et al.* have designed NIR-emitting MOFs using NIR-emitting Yb(III) lanthanide cations and phenylenevinylene dicarboxylate (PVDC) as a sensitizer-ligand for NIR imaging in living cells.[23] The sensitizers embedded in the nano-Yb-PVDC-3 MOF structure (Fig. 8a–c), formula $[Yb_2(PVDC)_3(DMF)_4]_n$, served as antennae as a result of the overlap between the excitation spectra of nano-Yb-PVDC-3 MOFs and the absorbance spectra of H_2-PVDC, which ensures the energy transfer from the excited sensitizer-ligands to the Yb(III) cations. NIR images demonstrated highly efficient discrimination between the nano-Yb-PVDC-3 MOFs and autofluorescence of cells, with emission visible from both the PVDC linker and the Yb(III) ion, providing efficient imaging despite the relatively low quantum yield of the MOFs in water that arises from the energy level of the –OH overtone vibration being so close to that of Yb(III) (Fig. 8d and e).

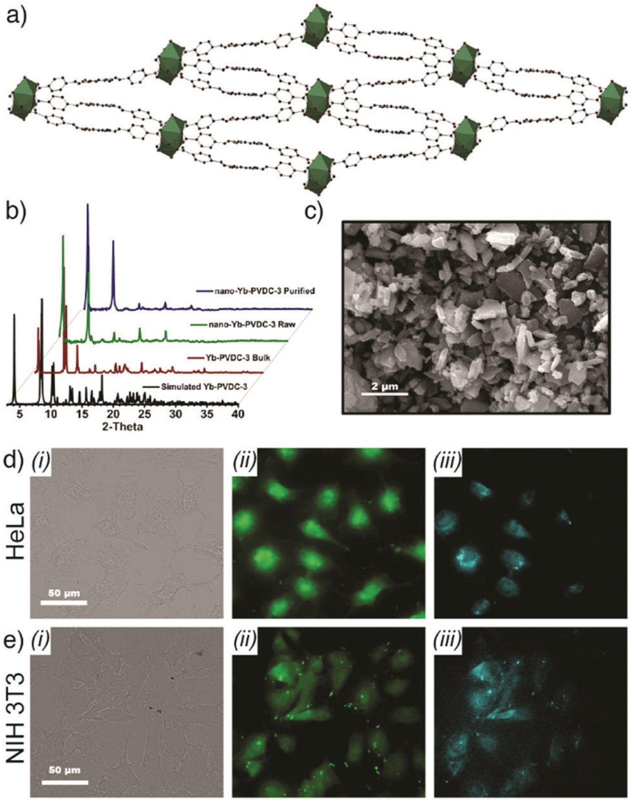

Fig. 8 (a) Crystal structure of Yb-PVDC-3. (b) Powder X-ray diffraction (PXRD) patterns of simulated and bulk Yb-PVDC-3 as well as as-synthesised and purified nano-Yb-PVDC-3. (c) SEM image of nano-Yb-PVDC-3. Visible and NIR microscopy images of nanoYb-PVDC-3 in (d) HeLa cells and (e) NIH 3T3 cells: (i) Bright-field, (ii) H_2-PVDC emission (λ_{ex} = 377/50 nm, λ_{em} = 445/50 nm), (iii) Yb(III) emission (λ_{ex} = 377/50 nm, λ_{em} = long pass 770 nm) images. Reproduced with permission.[23] Copyright (2013) National Academy of Sciences.

The colloidal stability of MOF nanoparticles is a challenging issue to overcome for their *in vivo* application. Park *et al.* reported a very facile solution to prepare water-dispersible luminescing MOFs using a simple hand-grinding technique. Tb-MOFs, composed of Tb(III) ions and tripodal carboxylate ligands such as triazine-1,3,5-tribenzoic acid, were stabilised by facile mechanical grinding with a biocompatible and biodegradable surfactant (Pluronic F127), a triblock copolymer composed of two poly(ethylene glycol) blocks at both of the termini of a poly(propylene oxide) block.[30] The particles were also employed as drug delivery agents by encapsulating the anticancer drug DOX, and acted as a multifunctional biomaterial, which demonstrated efficient cell imaging and cancer cell killing by drug delivery. In another study, Wang *et al.* reported multifunctional water-soluble $NaLnF_4$@MOF-Ln (Ln = Y, Tm, Yb, and Eu) nanocomposites with dual-mode luminescence by combining the anti-Stokes luminescence of $NaYF_4$:Tm(III)/Yb(III) nanocrystals with the Stokes luminescence of mesoporous lanthanide MOFs

(MOF-Y:Eu(III)), constructed from Ln(NO_3)$_3$ (Ln = 95% Y + 5% Eu) and BTC.[105] The resulting $NaYF_4$:Tm(III)/Yb(III)@MOF-Y:Eu(III) nanocomposites were coated by polyvinylpyrrolidone (PVP) to promote their cellular uptake and loaded with DOX. The $NaLnF_4$@MOF-Ln nanocomposites exhibited a unique anti-Stokes blue fluorescence and Stokes red fluorescence under laser excitation at a specific wavelength and showed bright blue emission in HeLa cells under a fluorescence microscope with a 980 nm source. DOX release studies revealed the pH-dependence of the drug release from the nanocarriers showing higher release rate in the simulated acidic cancer cell environment.

2.1.3. Combination with luminescent nanoparticles. In addition to organic fluorophores and luminescent metal ions, incorporation of luminescent nanoparticles to MOFs is another common approach to obtain luminescent MOF structures. Persistent luminescent nanoparticles (PLNPs),[74,75] upconversion nanoparticles (UCNPs)[76–78] and quantum dots (QD)[79] are the most popular emitting nanoparticles combined with MOFs.

Persistent luminescent nanoparticles. Among these luminescing structures, persistent luminescent nanoparticles (PLNPs) possess a unique optical phenomenon wherein continuous emission takes place for seconds or hours even after removal of the excitation source.[106] Based on these superiorities, Xie and co-workers have recently reported combination of ZIF-8 nanoparticles (tetrahedral zinc(II) ions connected by 2-methylimidazolate (mIm) linkers, formula $[Zn(mIm)_2]_n$) with chromium-doped zinc gallogermanate (ZGGO) near-infrared PLNPs. This results in a core–shell multifunctional nanoplatform emitting in the NIR spectral region of the optical spectrum, for elimination of autofluorescence and obtaining deep tissue penetration and low irradiation damage under *in vivo* conditions.[74] ZGGO@ZIF-8 particles were prepared by nucleation crystallization of a ZIF-8 shell on the surface of ZGGO particles. In the study, the PLNPs offered long-term NIR persistent luminescent signals for autofluorescence-free bioimaging with red-light-rechargeable properties while biocompatible ZIF-8 – a well-known pH responsive MOF – provided a shell structure to accommodate the fluorescent anticancer drug DOX (Fig. 9a). The fabricated ZGGO@ZIF-8-DOX multifunctional nanoplatform achieved dual imaging of 4T1 murine breast adenocarcinoma cells by DOX fluorescence and NIR persistent luminescence, and additionally acted as a pH-responsive drug delivery system. The particles showed quite high DOX loading (93.2%) and a drug release profile accelerated in acidic conditions, as well as effective *in vivo* tumour imaging (Fig. 9b–f) and suppression. Around the same time, Yang and co-workers prepared similar ZGGO@ZIF-8 materials, also by a surface adsorption induced self-assembly of MOFs on the ZGGO PLNPs, and generated comparable results, with enhanced luminescence in the acidic tumour microenvironment, and achieved tumour specific *in vitro* and *in vivo* imaging.[75] These closely related examples are typical of the incorporation of multiple imaging/therapeutic factors into one MOF-based DDS.

Upconversion nanoparticles. Luminescent UCNPs possess an advantageous optical characteristic in their conversion of long wavelength excitation (usually NIR) to short visible wavelength emission. This feature helps them provide deep light penetration in biological tissues, minimized background auto-fluorescence, narrow emission peaks, and high photostability.[76,107] The combination of MOFs with UCNPs can not only enable luminescence imaging but also prevent undesired tissue damage associated with UV excitation. These superiorities have driven researchers to construct upconversion NMOFs as optical imaging and drug delivery agents integrating the distinct advantages of both structures. For example, Chowdhuri *et al.* prepared upconversion NMOFs constructed by the direct coating of folic acid (FA)-encapsulated ZIF-8 on $NaYF_4$:Yb(III)/Er(III) UCNPs, as depicted in Fig. 10a.[76] X-ray diffraction (XRD) studies confirmed the successful combination of $NaYF_4$:Yb(III)/Er(III) UCNPs with ZIF-8, showing characteristic diffraction peaks of both nanoparticles (Fig. 10b), with a very small decrease in the initial optical intensity of UCNPs (Fig. 10c). The prepared UCNP@ZIF-8/FA nanocomposites were subsequently loaded with the anticancer drug 5-FU by adsorption

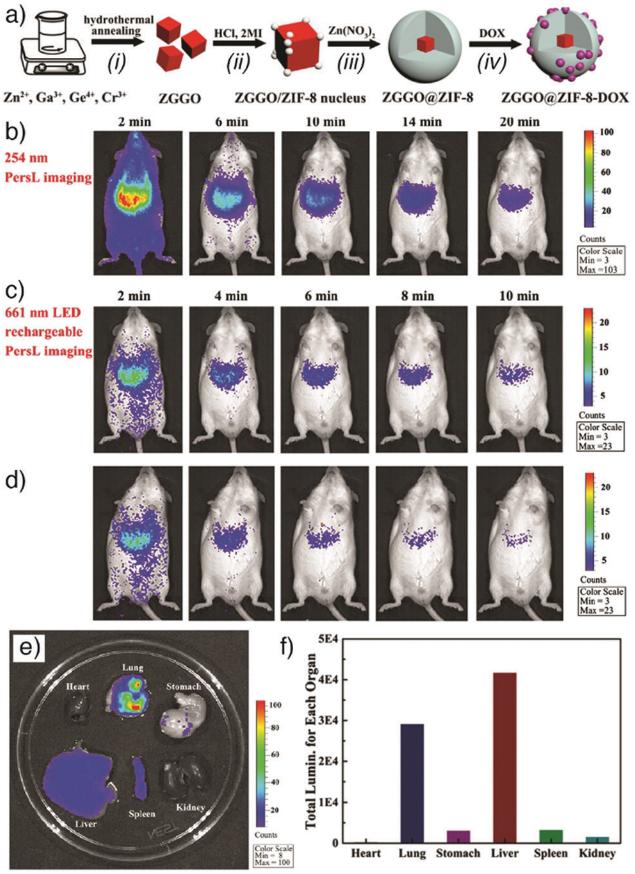

Fig. 9 (a) Schematic representations of (i)–(iii) the synthesis of core–shell ZGGO@ZIF-8 multifunctional nanoparticles and (iv) loading with anticancer drug DOX. (b) *In vivo* persistent luminescence imaging of a mouse, intravenously injected with ZGGO@ZIF-8 (0.2 mL, 1 mg mL^{-1} in PBS) under 254 nm irradiation for 5 min, (c) after *in situ* 661 nm LED recharging for 2 min, and (d) after a further interval of 10 min. (e) *Ex vivo* persistent luminescence imaging after 24 h administration, conducted after 661 nm LED recharging for 2 min and (f) the corresponding total luminescence of major organs in the mouse. Reproduced with permission.[74] Copyright (2018) American Chemical Society.

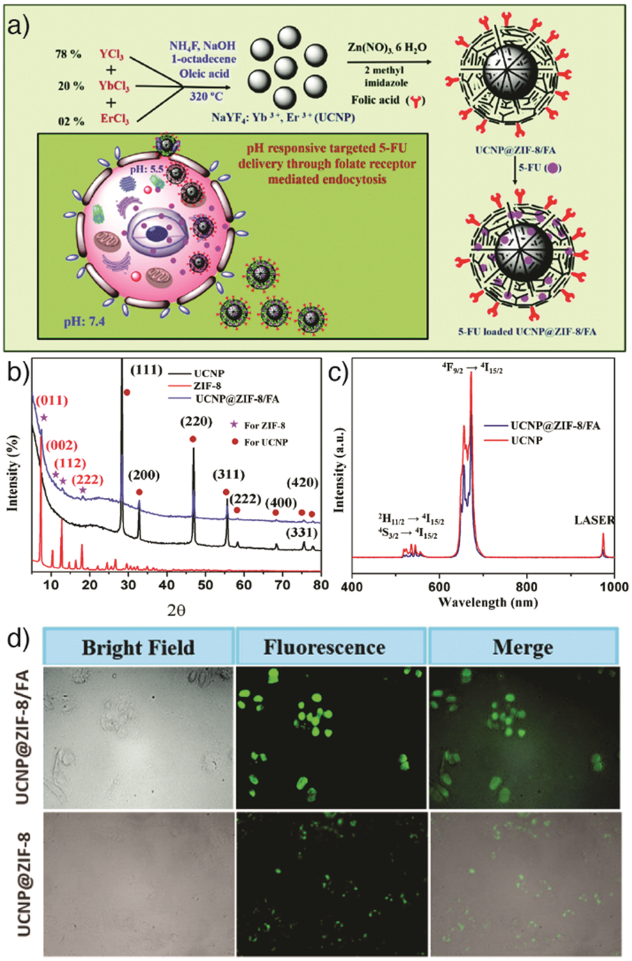

Fig. 10 (a) Schematic illustration of the synthetic route to FA encapsulated and 5-FU loaded upconversion MOF composites, 5-FU loaded UCNP@ZIF-8/FA, as a targeted and pH responsive anticancer drug delivery agent. (b) PXRD patterns of the fabricated UCNPs, ZIF-8, and UCNP@ZIF-8/FA. (c) Emission spectra of UCNP and UCNP@ZIF-8/FA (λ_{ex} = 980 nm). (d) Fluorescence microscopy images of HeLa cells incubated with 5 μg mL^{-1} of UCNP@ZIF-8/FA (upper) and UCNP@ZIF-8 (lower) for 6 h at 37 °C, with the corresponding bright field and overlay images. Reproduced with permission.[76] Copyright (2016) The Royal Society of Chemistry.

into the MOF nanostructure, which resulted in a high drug loading (685 mg g^{-1}). The upconversion NMOFs functioned efficiently as imaging agents, producing strong fluorescence signals under *in vitro* conditions with HeLa cells and the FA conjugated UCNP@ZIF-8 showed higher cellular penetration compared to the particles without FA (Fig. 10d). In addition, the as-prepared 5-FU loaded UCNP@ZIF-8/FA nanocomposites showed higher drug release in acidic conditions, suggesting a pH-responsive drug release from the structures, and also induced greater cytotoxicity towards HeLa cells than L929 mouse fibroblast cells due to the higher cellular internalization in HeLa cells though folate receptor (FR)-mediated endocytosis.

The group also reported the fabrication of $NaYF_4$:Yb(III)/Er(III) UCNPs combined with FA encapsulated UiO-66-NH_2 NMOFs (a structural analogue of UiO-66, where the linker is BDC-NH_2) using a similar synthetic approach and employed them as targeted drug delivery agents loading with DOX anticancer drug.[77] The obtained DOX loaded UCNP@UiO-66-NH_2/FA nanoparticles improved the therapeutic efficacy of DOX compared to UCNP@UiO-66-NH_2 by higher cellular uptake through FR-mediated endocytosis, and also enhanced the fluorescence imaging efficiency *in vitro*.

In another study, an *in situ* self-assembly strategy was reported by Yuan *et al.* to prepare upconversion NMOFs.[78] The strategy allowed the coating of positively charged UCNPs with different, negatively charged Zr-MOFs, including UiO-66, UiO-66-NH_2, MOF-801, and PCN-223, a 12-connected Zr-porphyrin MOF with formula $[Zr_6O_4(OH)_4(TCPP)_3]_n$, through electrostatic interactions. The homogeneous distribution of $NaYF_4$:Yb/Er UCNPs, composed of hexagonal $NaYF_4$ UCNPs, doped with Yb/Er (18/2 mol%), on the MOF surface enabled uniform upconversion luminescence (UCL) on the microscale or single-particle scale. This is promising in a wide range of applications including luminescence-monitored drug delivery, which was shown by DOX release from the nanocomposites, as well as photodynamic therapy, due to the high singlet oxygen generation efficiency of PCN-223@$NaYF_4$:Yb/Er nanocomposites under the excitation of 980 nm light, by the energy transfer from UCNPs to the TCPP linkers of PCN-223.

Quantum dots. Quantum dots (QDs) are semiconductor nanocrystals usually in the size range of 2–10 nm (10–50 atoms), with a structure between bulk and molecular forms, which enables size dependent fluorescence. Narrow photoluminescence bands, broad absorption windows, large molar extinction coefficients, low photobleaching, high quantum yield, and high chemical stability are the major advantages over conventional chromophores.[108,109] These remarkable features make them promising optical imaging agents in various application areas, and their combination with MOFs has therefore attracted great attention in recent years.[47,79,110,111] In particular, fluorescent carbon nanodots (C-dots) are a novel class of QDs and nanocarbons, displaying strong fluorescence intensity with high physicochemical stability and low toxicity compared with toxic metal-based QDs, which is highly relevant for biomedical use.[112] As an example, He *et al.* integrated these with MOF nanoparticles to obtain C-dot-encapsulated MOF nanocomposites for fluorescence imaging of cancer cells and simultaneous pH-responsive drug delivery.[79] The particles were prepared by directly mixing synthesized green fluorescent C-dots with $Zn(NO_3)_2{\cdot}6H_2O$ and 2-methylimidazole, the precursors to ZIF-8, at room temperature in methanol without stirring for 24 h. The fluorescence intensity and size of the resulting C-dots@ZIF-8 nanoparticles (NPs) were tuned by varying the amount of C-dots and the concentration of the precursors. The NPs were further loaded with 5-FU and employed as pH-responsive anticancer drug delivery vehicles with simultaneous fluorescence imaging of cancer cells (Fig. 11).

2.1.4. Two-photon responsive MOFs. Two-photon (TP) fluorescence imaging is a powerful imaging technique, in which fluorophores are excited by simultaneous absorption of two photons in the NIR region that results in emission of a single photon of higher energy in the visible spectrum, thereby

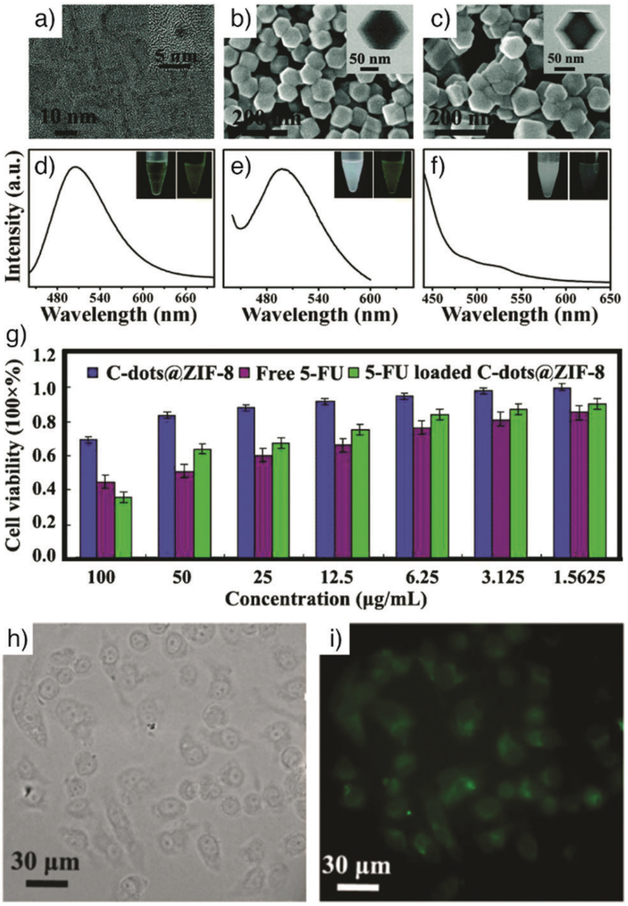

Fig. 11 (a) HRTEM image of C-dots (inset shows an HRTEM image of a single C-dot). SEM images of (b) C-dots@ZIF-8 and (c) ZIF-8 (insets represent the corresponding TEM images). Photoluminescence (PL) spectra of (d) bare C-dots, (e) C-dots@ZIF-8, and (f) pure ZIF-8 (λ_{ex} = 420 nm). Insets are the photographs of the corresponding samples suspended in methanol solution under ambient light (left) and under 365 nm UV light (right). (g) *In vitro* cytotoxicity of HeLa cells incubated with C-dots@ZIF-8, free 5-FU and 5-FU loaded C-dots@ZIF-8. (h) The differential interference contrast (DIC), and (i) confocal laser scanning microscopy (CLSM) images of HeLa cells incubated with 5-FU loaded C-dots@ZIF-8 for 24 h. Reproduced with permission.[79] Copyright (2014) The Royal Society of Chemistry.

allowing deeper tissue penetration and minimized tissue autofluorescence and photo-induced damage compared to conventional one-photon imaging techniques.[113–116] NMOFs with high porosity and periodic structures not only enable efficient loading of drugs but can also accommodate two-photon responsive chromophores. In addition, the photophysical properties of the imaging agents can be modified by the confinement effect in nanoscale pores, as reported by Maza *et al.* using UiO-67 doped with a photoactive metal polypyridyl complex of ruthenium(II) bis(2,2′-bipyridine)(2,2′-bipyridyl-4,4′-dicarboxylic acid) dichloride,[117] or ruthenium(II) bis(2,2′-bipyridine)(2,2′-bipyridyl-5,5′-dicarboxylic acid) dichloride,[118] which resulted in dramatic increase in luminescence lifetime of the Ru complexes.

Similarly, Chen *et al.* have incorporated the cationic ruthenium(II) tris(bipyridyl) complex, $[Ru(bpy)_3]^{2+}$, into UiO-67 MOFs for *in vitro* two-photon fluorescence (TPF) imaging and PDT.[119] The theranostic nanoparticles were prepared by soaking the UiO-67 nanoparticles in a DMF solution of $[Ru(bpy)_3](PF_6)_2$ at 90 °C. Trapping of the $[Ru(bpy)_3]^{2+}$ guest molecules in the MOF structures dramatically improved their quantum yield (Fig. 12a), luminescence lifetime (Fig. 12b), and TPF intensity (Fig. 12c) as a result of the steric confinement effect of MOF pores. The obtained nanoparticles, with an average diameter of ∼92 nm, showed improved stability upon light exposure, which resulted in a strong *in vitro* cell-killing effect and effective photodynamic therapy towards A549 human lung cancer cells by generating singlet oxygen upon non-invasive light irradiation, while exhibiting good biocompatibility without irradiation (Fig. 12d). Confocal laser scanning microscopy (CLSM) images confirmed that UiO-67-$[Ru(bpy)_3]^{2+}$ NPs were successfully internalized into A549 cells and demonstrated efficient *in vitro* TPF imaging capability with red fluorescence in the cytoplasm under 880 nm light irradiation (Fig. 12e and f).

In order to obtain more effective intracellular sensing and a deep tissue imaging agent, Yang *et al.* also integrated the advantages of two photon excitation with MOFs, obtaining a

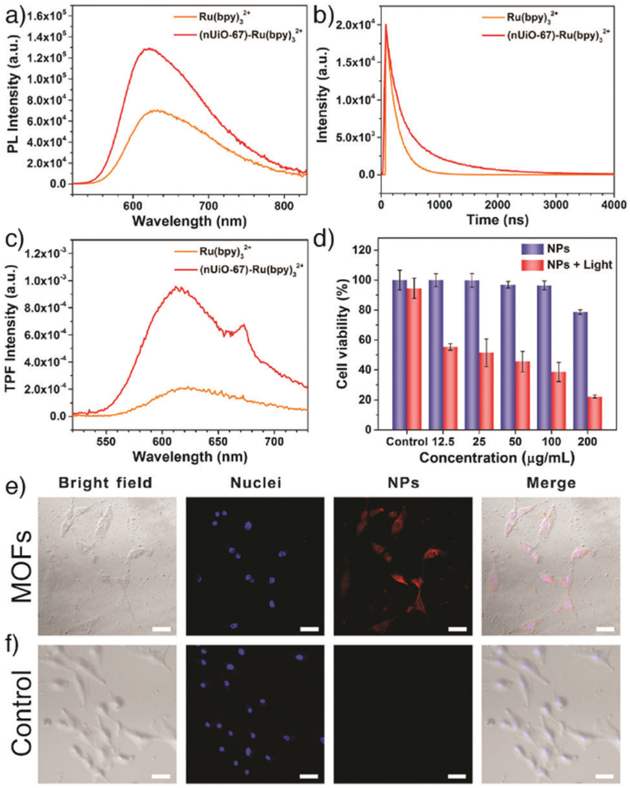

Fig. 12 (a) One-photon photoluminescence spectra, (b) time-resolved luminescence decay curves, and (c) two-photon fluorescence (TPF) spectra of $Ru(bpy)_3^{2+}$ and the (nUiO-67)-$Ru(bpy)_3^{2+}$ NPs. (d) Cell viability of A549 cells with/without light irradiation after being treated with (nUiO-67)-$Ru(bpy)_3^{2+}$ NPs at different concentrations (λ > 400 nm, 200 mW cm^{-2}, 10 min). CLSM images of A549 cells (e) treated with (nUiO-67)-$Ru(bpy)_3^{2+}$ NPs (upper) and (f) untreated (lower) for 12 h. Blue fluorescence indicates Hoechst 33342 nuclei staining. Red shows nanoparticles (λ_{ex} = 880 nm, λ_{em} = 580–660 nm). The scale bar is 50 μm. Reproduced with permission.[119] Copyright (2017) American Chemical Society.

TP-MOF composite to detect H_2S or Zn(II) as model analytes in living tissues, and also to visualize tissues.[120] PCN-58, a bis-azidomethyl functionalised analogue of the large-pore Zr MOF UiO-68 comprised of 2′,5′-bis(azidomethyl)-[1,1′:4′,1″-terphenyl]-4,4″-dicarboxylate, (TPDC-$2CH_2N_3$) coordinated with Zr_6 clusters, can be conjugated with target-responsive two-photon organic moieties by Cu(I)-catalysed azide–alkyne cycloaddition (CuAAC) without any cross reactivity towards the MOF structure itself. PCN-58 was reacted with 6-amino-2-(prop-2-yn-1-yl)-1*H*-benzo[*de*]isoquinoline-1,3(2*H*)-dione (alkynyl-BR-NH_2) and then the amino group of the structure turned into an azide group by the use of *tert*-butyl nitrite and trimethylsilyl azide to obtain probe 1 for H_2S detection. To achieve probe 2 for Zn(II) detection, PCN-58 was reacted with 2-(bis(pyridin-2-ylmethyl)amino)-*N*-(1,3-dioxo-2-(prop-2-yn-1-yl)-2,3-dihydro-1*H*-benzo[*de*]bisoquinolin-6-yl) acetamide (alkynyl-DL). The constructed TP-MOF probes containing the different two-photon fluorophores were successfully employed in live cells and tissue slices (rat liver and lung tissue), using two-photon microscopy (excited at $\lambda \sim$ 820 nm) with a tissue penetration depth of 130 μm to detect H_2S and Zn(II), as well as visualize tissues.

Cumulatively, these examples of emissive MOFs and composites highlight the wide range of strategies available to prepare materials for biological imaging. The use of intrinsically luminescent linkers, such as porphyrins, is highly attractive for its simplicity, but many organic fluorophores do not possess highly symmetric structures, which is often a requirement for synthesis of ordered, porous MOFs. Likewise, the coordination chemistry of the lanthanides, which is dominated by steric factors, often results in denser structures with limited porosity. Hence, for combined imaging and drug delivery, postsynthetic incorporation or hybridisation with fluorophores is often the more advantageous approach.

2.2. Magnetic resonance imaging

Magnetic resonance imaging (MRI), founded on the principles of nuclear magnetic resonance (NMR), has become an essential tool for clinical diagnosis over the past few decades. MRI is a non-invasive imaging modality that uses non-ionizing radiation in the radio frequency range and does not employ any radio-isotopes, unlike computed tomography and traditional X-rays. It offers harmless tissue imaging with high spatial resolution and tissue contrast, and superb depth of penetration. MRI detects spin reorientation in a magnetic field, and hence provides detailed anatomic images of soft tissues with 3D imaging capability, such as imaging of the brain, heart, and cartilage, as well as detection of tumours and the assessment of therapeutic responses.[121,122] MRI signals are produced by the NMR signals of the water protons (^1H nuclei) in a specimen.[38] However, the intrinsic low signal difference between diseased and normal tissues can be insufficient to detect lesions.

To enhance the signal differences between the tissues, MRI contrast agents have been developed to improve the contrast at the region of interest by altering the magnetic fields and accelerating relaxation processes. In the absence of an external magnetic field, the magnetic moments of ^1H nuclei are randomly oriented. However, in the external magnetic field of an MRI scanner, the magnetic moments of ^1H nuclei are aligned through an applied radio frequency pulse. Upon the removal of radio frequency perturbation, the ^1H nuclei undergo a recovery process which usually occurs by two different types of relaxation time: longitudinal relaxation, characterized by the parameter T_1 (spin–lattice relaxation time), and transverse relaxation, characterized by the parameter T_2 (spin–spin relaxation time).[123,124] Depending on the type of the relaxation time, the contrast agents are sorted into two main categories: T_1 agents shorten the longitudinal (spin–lattice) relaxation time of the surrounding water protons, and provide a positive contrast and brighter MRI images, whereas T_2 agents shorten the transverse (spin–spin) relaxation time of the water protons and create a negative, dark contrast effect.[121,123] The efficiency of a contrast agent is determined by the ratio between transverse (r_2) and longitudinal (r_1) relaxivity values, which are defined as the slope of a plot of $1/T_2$, and the slope of a plot of $1/T_1$ *vs.* the concentration, respectively.[125] A lower value of r_2/r_1 (between 1 and 3) indicates T_1 type, while higher values (>10) indicate T_2 type. Between these values, the materials can show dual contrast characteristics.[126]

MRI is a powerful imaging modality, however it requires the administration of contrast agents in large doses to enable adequate MRI contrast in target tissues.[38] For clinical applications, the most widely used MRI contrast agents are paramagnetic gadolinium (Gd) chelates, which act as T_1 contrast agents producing signal enhancement in T_1-weighted images.[127–129] Small molecule Gd chelates show modest r_1 values ($\sim$4–5 mM^{-1} s^{-1}), so require high doses for an effective contrast. Moreover, the release of free Gd ions from unstable Gd complexes has been associated with nephrogenic systemic fibrosis in renal failure patients and the use of some of the gadolinium based contrast agents was banned in Europe in spring 2007.[127,128,130–133] However, the use of the most stable gadolinium-based contrast agents at the lowest possible dose has been mostly commonly accepted as the optimal protocol.[131,134]

Recently, NMOFs have become a promising alternative to Gd complexes as potential MRI agents, due to their large metal payload, low toxicity, superior stability, and higher relaxivity values, which provide stronger contrast enhancement with lower doses and hence improve diagnostic sensitivity.[53] MOF contrast agents can be designed either as T_1, T_2 or combined T_1 and T_2 contrast agents by building the structure with MRI active paramagnetic metals as intrinsic components, or combining synthesized MOFs with various MRI contrast agents. Furthermore, they can be simultaneously utilized as drug delivery agents, and directed to a specific area interested in the body by conjugation of various cell targeting ligands.[135] Gd-Based MOFs, Mn-based MOFs and Fe-based MOFs have been developed as promising candidates as MRI contrast agents in the literature.[28,136–138]

2.2.1. Gd-Based MOFs. Gadolinium metal organic frameworks (Gd-MOFs) have emerged as an alternative to Gd chelates to enhance the per-metal-based relaxivity values of Gd complexes and decrease the concentrations used in imaging applications.[22,28,40] Gd-MOF nanoparticles were used as MRI contrast agents for the first time by Lin and co-workers in

2006.[28] The two MOFs used in the study were synthesized by a reverse microemulsion technique. $[Gd(BDC)_{1.5}(H_2O)_2]_n$ nanorods of different sizes resulted from the combination of $GdCl_3$ and bis(methylammonium) benzene-1,4-dicarboxylate in the cationic cetyltrimethylammonium bromide (CTAB)/isooctane/1-hexanol/water system, while mixing $GdCl_3$ and tri-(methylammonium) benzene-1,2,4-tricarboxylate (1,2,4-BTC) in the CTAB/isooctane/1-hexanol/water microemulsion system resulted in crystalline nanoplates of $[Gd(1,2,4\text{-}BTC)(H_2O)_3]_n$, with a diameter of ∼100 nm and an average thickness of 35 nm. Both NMOFs showed very high r_1 and r_2 relaxivities on a per mM of Gd(III) basis and extraordinarily high r_1 and r_2 relaxivities on a per mM of nanoparticle basis. In 2008, the group showed surfactant-assisted synthesis of two novel nanoscale Gd-MOFs, block-like particles of $[Gd_2(BHC)(H_2O)_6]_n$ with a fluorite topology and $[Gd_2(BHC)(H_2O)_8]_n$ with an inverse rutile topology (BHC stands for benzene-1,2,3,4,5,6-hexacarboxylate) at elevated temperatures by controlling the pH values of the reaction medium.[40] Particles of $[Gd_2(BHC)(H_2O)_6]_n$ showed a modest longitudinal relaxivity (r_1) of 1.5 mM^{-1} s^{-1}, but significantly high transverse relaxivity (r_2) value of 122.6 mM^{-1} s^{-1} on a per-Gd basis, providing a strong contrast in magnetic resonance.

Hatakeyama *et al.* reported the control of size and shape by incorporation of hydrotropes into the reverse microemulsion synthesis of Gd-MOF nanoparticles with a general composition of $[Gd(1,4\text{-}BDC)_{1.5}(H_2O)_2]_n$ and $[Gd(1,2,4\text{-}BTC)(H_2O)_3]_n$.[22] Hydrotropes are defined as compounds that offer both hydrophobic and hydrophilic features. Specifically, sodium salicylate, used amongst various hydrotropes in the study, exhibited the best size reduction, producing Gd-MOF nanoparticles of an average size of 82 nm with the highest total surface area. The increase in the outer surface areas of the nanoparticles provided enhanced longitudinal relaxivity values (r_1) up to 83.9 mM^{-1} s^{-1}, which is nearly 20 times higher than that of Magnevist (gadopentetate dimeglumine), a clinical positive contrast agent used for comparison in the study. Wang *et al.* reported the preparation of NMOF-based T_1–T_2 dual-modal contrast agents for MRI by using a mixture of Eu(III) and Gd(III) as metallic nodes, isophthalic acid (H_2IPA) as building blocks, and PVP as a surfactant. The produced spherical Eu,Gd-NMOFs were also coated by a silica layer to improve the particle stability and functionalized with c(RGDyK), a tumour-targeting peptide sequence, which targets integrin $\alpha_v\beta_3$.[19] The Eu,Gd-NMOF@SiO_2 nanoparticles showed high longitudinal (38 mM^{-1} s^{-1}) and transversal (222 mM^{-1} s^{-1}) relaxivities by inducing signal enhancement on T_1- and signal attenuation on T_2-weighted images when injected *in vivo*.

2.2.2. Mn-Based MOFs. Paramagnetic Mn(II) ions are known as potent T_1 MRI contrast agents, functioning similarly to gadolinium but showing less toxicity.[139,140] Mn also possesses a minor T_2 effect by causing darkening in MR images. Mn(II) ions are natural cellular constituents involved in mitochondrial processes, which makes their uptake highly dependent on mitochondrial metabolism and mitochondrial density in the cells, and they can be an effective contrast agent for the liver and other mitochondria-rich organs like the pancreas and the kidneys.[121,139] These characteristics have directed researchers to develop Mn-based MOFs.[21,141,142] Lin's group reported the synthesis of $[Mn_3(BTC)_2(H_2O)_6]_n$ with controllable morphology using reverse-phase microemulsion procedures, subsequently coating the Mn MOFs with a silica layer and functionalizing with a cyclic arginine–glycine–aspartate (RGD) peptide for cancer targeting. The yielded nanostructures demonstrated target-specific MRI providing high contrast enhancement.[21] In another study, Yang *et al.* showed the construction of a new type of nanoscale metal–organic particles (NMOPs) *via* self-assembly of Mn(II) ions and a NIR dye, IR825, as bridging ligand, which were further encapsulated within a polydopamine (PDA) shell and functionalized with PEG, for imaging-guided photothermal cancer treatment.[141] The produced multifunctional particles offered strong contrast in T_1-weighted MRI owing to Mn(II) in the structure of Mn-IR825@PDA-PEG NMOPs, while IR825 with strong NIR absorbance enabled efficient photothermal conversion ability and high efficacy of photothermal therapy (PTT) upon 808 nm laser irradiation, as well as a great photostability under both *in vitro* and *in vivo* conditions.

Qin *et al.* reported the synthesis and comparison of two water-stable Mn- and Gd-based MOFs of *N*-(4-carboxybenzyl)-(3,5-dicarboxyl)pyridinium bromide ($H_3CmdcpBr$), $([Mn_2(Cmdcp)_2(H_2O)_2]\cdot H_2O)_n$ (1) and $([Gd(Cmdcp)(H_2O)_3](NO_3)\cdot 3H_2O)_n$ (2), and showed their applications as strong MRI contrast agents under *in vivo* conditions.[142] The *in vitro* characterization demonstrated that the Mn-based MOF possessed a slightly higher relaxivity r_1 value (17.50 mM^{-1} s^{-1}) compared with the Gd-based analogue (13.46 mM^{-1} s^{-1}), and both of them are superior to that of the clinical positive contrast agent, Gd–DTPA (DTPA = diethylene triamine pentaacetate, r_1 = 4.87 mM^{-1} s^{-1}) used as a control in the study (Fig. 13a and b). *In vivo* MR images of the Mn-based MOF indicated that the nanoparticles have high contrast efficacy over a prolonged timeframe enabling remarkable positive signal enhancement in kidneys (Fig. 13c).

2.2.3. Fe-Based MOFs. Iron is one of the essential elements in living organisms that is presented in abundance and has fundamental and important roles in many different biological processes, unlike gadolinium.[143] Due to the high concentration of iron in the body, the potential leakage of the element from the MOF structures is not expected to cause any significant damage and any free Fe to be metabolically eliminated.[122] As opposed to Gd and Mn, iron-based MRI contrast agents increase the rate of T_2 relaxation and exhibit a negative image enhancement, leading to dark contrast effects in MR images. The MIL family of MOFs constructed from iron(III) and carboxylate linkers have been shown to act as strong T_2-weighted MRI contrast agents in several studies.[31,32] The pioneering work on the development of iron-based MOFs as MRI contrast agents was reported by Horcajada *et al.* in 2010.[31] Non-toxic MIL-88A(Fe), where iron(III) trimers, are connected by fumarate linkers into a flexible hexagonal structure with composition $[Fe_3O(fum)_3(H_2O)_2X]_n$ (X is a monocounterion typically OH^- or Cl^-), and MIL-100(Fe) were synthesized in biologically and environmentally favourable aqueous or ethanolic media, exhibit high transversal (r_2) relaxivities. Further functionalization of the particles by a

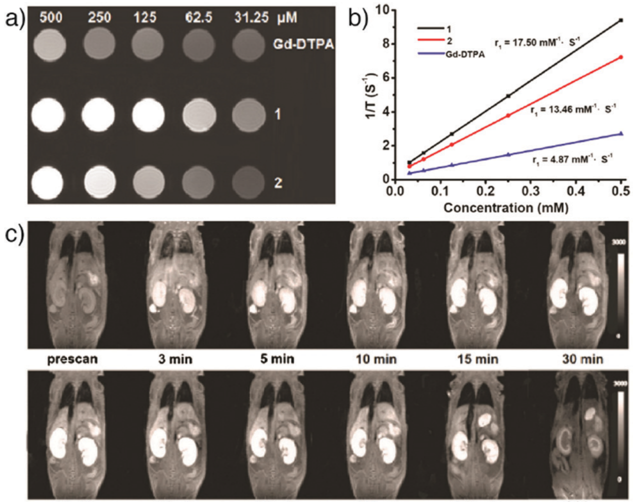

Fig. 13 (a) T_1-Weighted MR images of $([Mn_2(Cmdcp)_2(H_2O)_2]\cdot H_2O)_n$ (1) and $([Gd(Cmdcp)(H_2O)_3](NO_3)\cdot 3H_2O)_n$ (2), as well as the commercial contrast agent Gd–DTPA, at different concentrations in water. (b) The plot of $1/T_1$ *vs.* the concentrations for each. (c) MR images of a female nude mouse displaying the MR signal intensity in both kidneys at different time points of intravenous post-injection with $([Mn_2(Cmdcp)_2(H_2O)_2]\cdot H_2O)_n$. Reproduced with permission.[142] Copyright (2017) American Chemical Society.

H_3C–PEG–NH_2 coating increased the r_2 values from 56 to 95 s^{-1} mM^{-1} for MIL-88A(Fe), and from 73 to 92 s^{-1} mM^{-1} for MIL-100(Fe), by decreasing the aggregation of the MOFs in water. Zhang *et al.* demonstrated an alternative application with MIL-101(Fe) nanoparticles, in which the MOFs were utilized for delivery of unmethylated cytosine–phosphate–guanine oligonucleotides (CpG ODNs) to induce immune response in combination with MRI.[32] MIL-101(Fe) nanoparticles were post-synthetically modified with CpG ODNs by π–π interactions. The nanoconjugates showed stronger immune response than free CpG ODNs, and high T_2-MRI capacity both *in vitro* and *in vivo*, providing promising proof-of-concept as immunostimulatory and imaging. In another study, Fe-based MOF contrast agents were constructed by chelating Fe(III) ions with a polydopamine coating on the DOX loaded Zn-MOF, ZIF-8, synthesized *via* a one-pot synthesis process.[144] The ZIF-8 nanoparticles were further conjugated by hyaluronic acid (HA), through iron-mediated coordination, for targeted drug delivery and MRI in CD44 (a cell surface HA-binding glycoprotein) overexpressed prostate cancer cell line (PC-3). The multifunctional ZIF-8 nanoparticles showed efficient intracellular uptake, and *in vitro* chemotherapeutic efficacy compared to free DOX as well as favourable contrast ability for MRI from the conjugated Fe(III) ions.

An alternative and effective strategy to design Fe-based MOFs for MRI is to encapsulate superparamagnetic iron oxide nanoparticles (SPIONs) into MOFs. SPIONs are clinically used MRI contrast agents with an extraordinary ability to shorten T_2 relaxation times due to their unique magnetic properties.[121,136,145] Zhao *et al.* reported novel theranostic Fe_3O_4@UiO-66 core–shell composites, fabricated by *in situ* growth of a UiO-66 MOF shell on a Fe_3O_4 core, for drug delivery *via* UiO-66 and simultaneous MRI by the Fe_3O_4 nanoparticles (Fig. 14a).[136] The decrease in BET surface area (S_{BET}) of UiO-66 MOFs confirmed the interior Fe_3O_4 core within UiO-66 (Fig. 14b) while the high saturation magnetization (M_s) value showed their superparamagnetic characteristics (Fig. 14c). The core–shell nanoparticles served as excellent T_2 contrast agents with a high transverse relaxivity (255.87 mM^{-1} s^{-1}) and significant darkening effect in HeLa cells at increased concentrations (Fig. 14d), as well as *in vivo* MRI capability in Kunming mouse and HeLa-tumour bearing mice at increased incubation times (Fig. 14e and f). Furthermore, the particles could be loaded with DOX for simultaneous cancer therapy, and the obtained Fe_3O_4@UiO-66-DOX particles exhibited high cell mortality and remarkable tumour size inhibition compared with Fe_3O_4@UiO-66, both *in vitro* and *in vivo*.

In another study, Chowdhuri *et al.* showed the development of a new magnetic porous system constructed by coating of superparamagnetic Fe_3O_4 nanoparticle cores by a shell of IRMOF-3, which is constructed from octahedral Zn clusters and BDC-NH_2 with formula $[Zn_4O(BDC\text{-}NH_2)_3]_n$, for MRI.[145] The nanoparticles were further functionalized by conjugation of a cancer targeting ligand, folic acid, and a fluorescent molecule, rhodamine B isothiocyanate, for simultaneous fluorescence imaging. After loading with the anticancer chemotherapy drug paclitaxel, through hydrophobic interactions, the NMOFs showed good therapeutic efficacy in HeLa cells, by high internalization *via* receptor-mediated endocytosis, and strong T_2-weighted MRI contrast due to the high loading amount of MR-active Fe_3O_4 nanoparticles. These latter examples show that the MOF/nanoparticle hybrid route is an attractive alternative to preparing MOFs with intrinsically magnetically active metals, but the protocol does require additional synthetic steps and additional components, which may complicate large scale manufacture of any clinical MOF-based MRI contrast agents.

2.3. Computed tomography

Computed tomography (CT) is a non-invasive medical imaging technique for 3D visualization of internal structures with high spatial and temporal resolution. CT is based on the attenuation of X-rays, which mainly uses contrast agents with high atomic numbers (high-Z elements) showing high X-ray attenuation ability, such as iodine, gold, barium, bismuth and gadolinium. The attenuation values of most tissues are similar, which makes the differentiation of diseased from normal tissue difficult. However, by using contrast agents containing heavy elements, the desired contrast enhancement can be achieved.[33,146,147] Currently available contrast agents in clinical practice are mostly iodine derivatives that may cause severe side effects, like thyroid dysfunction or renal toxicity, due to small amounts of free iodine in the formulation.[148,149] In addition, these materials show non-specific distribution and rapid pharmacokinetics, and therefore require administration in high concentrations for enhanced CT imaging resolution.

To overcome these limitations, a number of MOF nanoparticles containing high-Z elements have been recently developed and employed as potential CT contrast agents. For example, Lin's

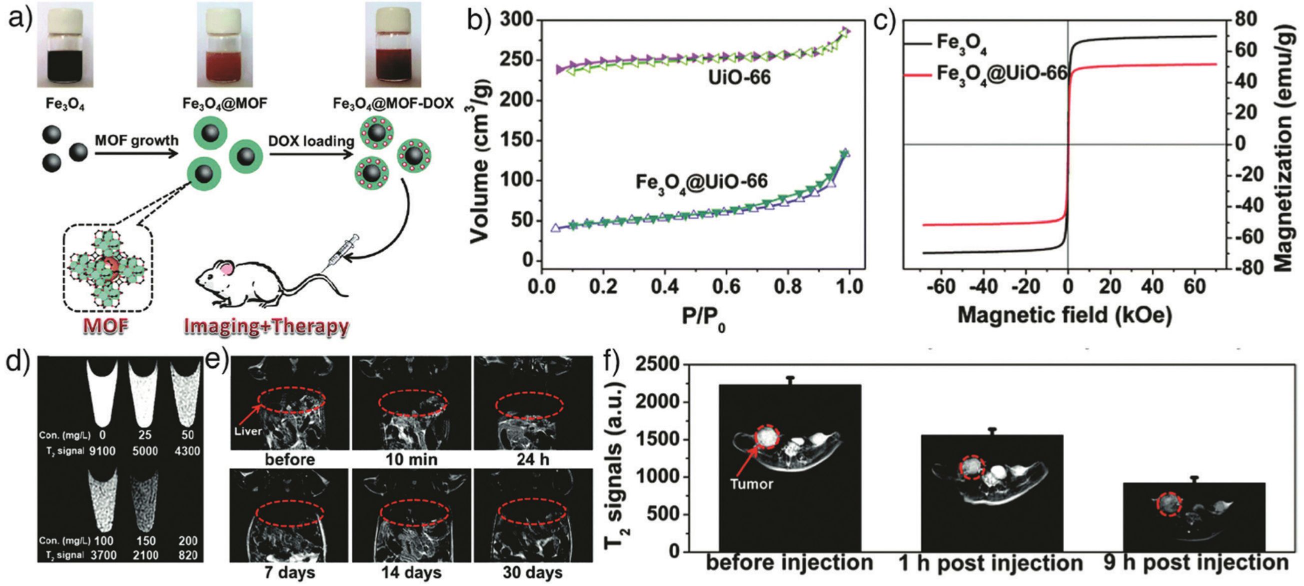

Fig. 14 (a) Schematic illustration for the preparation of theranostic Fe_3O_4@UiO-66 core–shell composites. (b) N_2 adsorption–desorption isotherms and (c) magnetization hysteresis curves of UiO-66 and Fe_3O_4@UiO-66 nanoparticles, confirming effective hybridisation. (d) *In vitro* T_2-weighted MR images of HeLa cells incubated with different concentrations of Fe_3O_4@UiO-66 composites (0, 25, 50, 100, 150 and 200 mg L^{-1}) for 24 h and enhanced darkening effect by concentration increase. (e) *In vivo* T_2-weighted MR images of a Kunming mouse injected with the composites and the images at different time points (red cycles show the liver region). (f) T_2-Weighted MR images of HeLa tumour-bearing mice before and at 1 h and 9 h post-intravenous injection with Fe_3O_4@UiO-66 (red cycles show the tumour region). Reproduced with permission.[136] Copyright (2016) The Royal Society of Chemistry.

group reported the construction of UiO-66 type NMOFs containing high-*Z* elements (zirconium and hafnium) and showed their applications as CT contrast agents.[42,150] Zr and Hf have high atomic numbers of 40 and 72, respectively, making them potential CT contrast agents. In the study, as-synthesized UiO-66(Hf) nanoparticles were further coated with silica and PEG in order to improve biocompatibility, and were employed for *in vivo* CT imaging of mice, which resulted in higher attenuation in the liver and spleen.[42] Zhang *et al.* developed the concept by the synthesis of an iodine-boron-dipyrromethene (BODIPY)-containing MOF, named UiO-PDT, as a CT imaging agent.[33] The nanocrystals were functionalised by exchanging the diiodo-substituted monocarboxyl-functionalized BODIPY (I2-BDP) with BDC linkers at the surfaces of pre-synthesised UiO-66. The obtained UiO-PDT nanocrystals exhibited no obvious severe acute or sub-acute toxicity, even at high injection dosages, and provided good X-ray attenuation – particularly for about 24 h after intravenous administration – as well as high accumulation in the tumour region of Sprague-Dawley rats bearing hepatomas (Fig. 15). In principle, any MOF nanoparticle containing high-*Z* elements in the linker, metal clusters, or surface functionality could be applied to CT imaging.

2.4. Positron emission tomography

Positron emission tomography (PET) is a commonly used non-invasive imaging modality that diagnoses abnormalities at the cellular/molecular level and provides 3D images with high sensitivity, specificity and limitless depth of penetration.[151] PET requires internal administration of a molecule labelled with a positron-emitting radionuclide known as radiotracer (usually at nanomolar concentrations) into the bloodstream of the patient. Various positron-emitting radionuclides, including ^{18}F ($t_{1/2}$ = 109.8 min), ^{11}C ($t_{1/2}$ = 20.39 min), ^{13}N ($t_{1/2}$ = 9.965 min), ^{15}O ($t_{1/2}$ = 2.037 min), ^{68}Ga ($t_{1/2}$ = 68 min), ^{64}Cu ($t_{1/2}$ = 12.7 hours), ^{89}Zr (3.27 days) and ^{124}I ($t_{1/2}$ = 4.176 days), are used for PET imaging in clinical applications.[152,153] The natural decay of the radionuclide comprises emission of a positron from the structure and interaction of this emitted positron with a free or loosely bound electron after it travels only a short distance through the tissue. Ultimately, one positive electron is annihilated with one negative electron, producing two photons which are given off in opposite directions with a 511 keV energy.[153] These high-energy gamma-rays are detected with a PET scanner, and the distribution of the radiotracer throughout the patient's body is constructed as a series of 3D images.

Based on these advantages, Hong and co-workers reported the application of NMOFs as a radiotracer by developing an intrinsically radioactive UiO-66 NMOF (^{89}Zr–UiO-66) through incorporation of a positron-emitting isotope of zirconium, zirconium-89, during the synthesis.[34] The particles were loaded with DOX, and then further surface engineered with pyrene-derived polyethylene glycol (Py–PGA–PEG) and an F3 peptide ligand, to target nucleolin on tumour cells and enhance the cellular uptake and drug delivery of the NMOFs in tumour region (Fig. 16a). The particles showed strong radiochemical and material stability in different biological media, as well as relatively high drug loading capacity (1 mg DOX per mg UiO-66), allowing them to be used as both a therapeutic agent

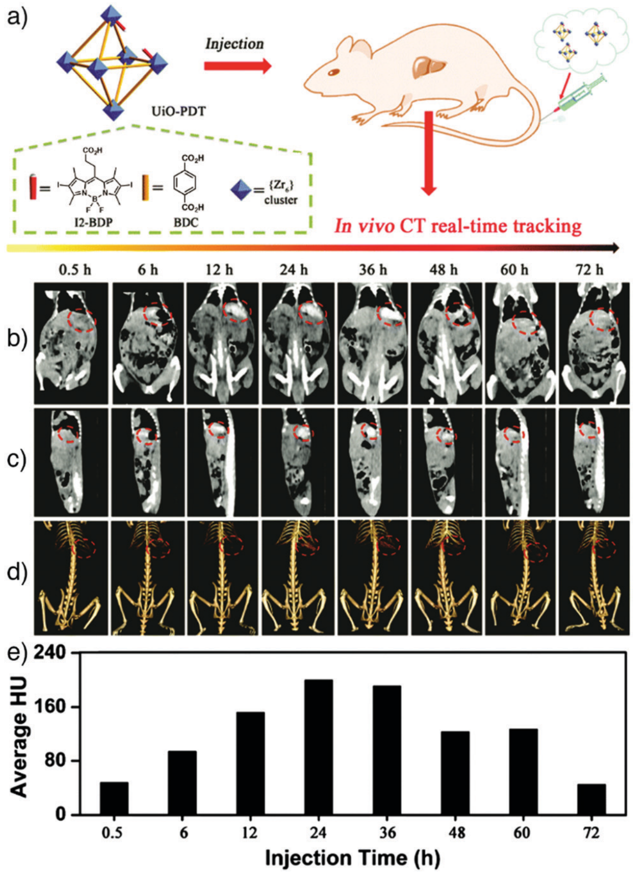

Fig. 15 (a) Schematic representation of the construction of UiO-PDT nanostructures as X-ray CT imaging agents. *In vivo* CT images of a Sprague-Dawley rat at different time points after being injected with UiO-PDT showing the (b) ventral, and (c) the lateral sides of the rat. (d) 3D images revealing the ventral sides of hepatic tumours, highlighted with red circles. (e) The corresponding Hounsfield unit values indicating the quantity of the attenuated signal. Reproduced with permission.[33] Copyright (2017) The Royal Society of Chemistry.

and a fluorescence visualizer. By conjugation of F3 targeting peptides, selective and enhanced uptake of ^{89}Zr–UiO-66 conjugates towards MDA-MB-231 human breast tumour cells was reported *via* PET images taken at different time points after injection of MDA-MB-231 tumour bearing mice with the nanoparticles (Fig. 16b). The results were further confirmed by *ex vivo* organ distribution studies obtained by tissue gamma-counting (Fig. 16c) and by *ex vivo* fluorescence imaging of DOX in tumour-bearing mice.

In another example, Liu's group reported the synthesis and use of ^{64}Cu radiolabelled and DOX loaded amorphous zeolitic imidazolate framework-8 (AZIF-8) to investigate how particle size affects the *in vivo* distribution of particles and their tumour targeting ability, using an *in vivo* quantitative tracing strategy based on PET imaging.[154] The nanoparticles were synthesized in different sizes by a rapid one-pot aqueous approach. To label the particles with ^{64}Cu, a chelator-free radiolabelling method, which relies on doping of the structure by ^{64}Cu(II) ions in the synthesis, was conducted. The results showed that the intracellular drug release rate increases as the size decreases, but CT imaging shows smaller MOF nanoparticles (60 nm) circulate in the blood longer and achieve over 50% higher tumour accumulation than larger MOFs (130 nm), providing higher antitumour efficacy.

2.5. Photoacoustic imaging

Photoacoustic imaging (PAI), also known as optoacoustic imaging, is a robust, non-invasive and non-ionizing biomedical imaging technique that uses both optical and ultrasonic imaging to visualize anatomical structures and physiological changes in biological tissues. This hybrid imaging modality has received great attention by effectively combining the high optical contrast of optical imaging with the high penetration depth and ultrasonic spatial resolution of ultrasound imaging.[155,156] In PAI, tissue is illuminated by short laser pulses, which cause a fast local temperature increase as a result of the absorption of the incident energy and, consequently, formation of a small and localized thermal perturbation. This leads to generation of photoacoustic (PA) pressure waves, which propagate inside the tissue owing to thermal expansion, and these photoacoustic signals can be detected with wideband ultrasound transducers. By measuring the duration and arrival time of the pressure pulses to the transducer, the location and size of the target tissue can be

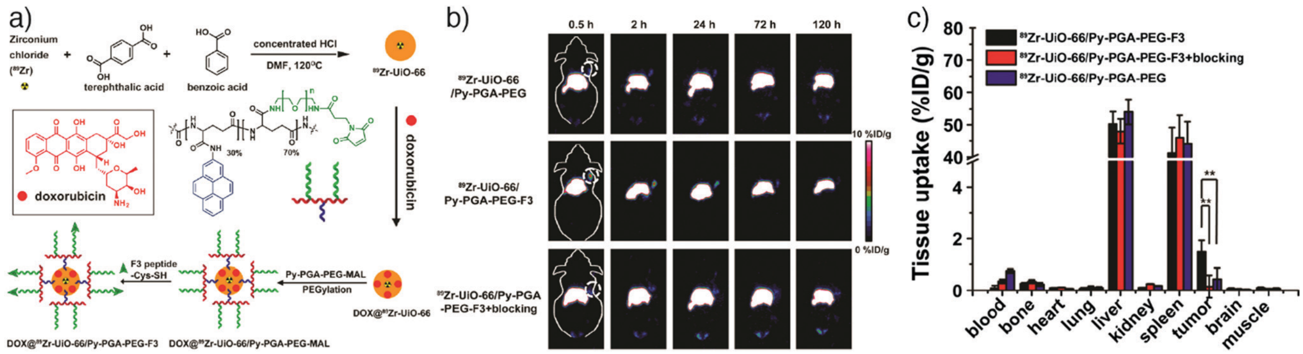

Fig. 16 (a) Scheme for the synthesis for ^{89}Zr-UiO-66/Py–PGA–PEG-F3 conjugates. (b) Coronal PET images of MDA-MB-231 tumour bearing mice at different time points after being injected with ^{89}Zr-UiO-66/Py–PGA–PEG-F3, ^{89}Zr-UiO-66/Py–PGA–PEG, and ^{89}Zr–UiO-66/Py–PGA–PEG-F3 with excess F3 peptide for blocking. (c) The corresponding organ distribution at 120 h post-injection obtained by tissue gamma-counting. $^{**}P < 0.01$. Reproduced with permission.[34] Copyright (2017) American Chemical Society.

determined.[157] In PA imaging, the sensitivity and specificity of the image usually depends on the endogenous contrast. However, the low intensity of internal PA signals in some tissues limits the possibility of obtaining high contrast PA images. Exogenous contrast agents have therefore been used to improve the image quality by PA signal and imaging contrast enhancement. Specifically, carbon nanotubes and noble metal nanoparticles – in particular gold nanoparticles (AuNPs) and gold nanorods (AuNRs) – have been popular in PAI, since they possess strong light absorption ability due to their enhanced surface plasmon resonance.[158,159]

NMOFs have been recently utilized as PAI contrast agents in several studies due to their attractive characteristics such as high porosity, tunable pore size, abundant metal sites and high-guest molecule loading capacity, which allow them to be designed as efficient PA contrast imaging agents as well as therapeutics by simultaneously delivering various drug molecules. For example, Chen and co-workers reported the fabrication of multifunctional MOF nanoparticles for PAI-guided chemo-/photothermal simultaneous tumour therapy by using MIL-100(Fe).[20] The Fe MOF nanoparticles were efficiently loaded with curcumin, as a chemotherapeutic agent, and coated with polydopamine (PDA) to achieve photoacoustic contrast and photothermal conversion properties, and enhance the colloidal stability and biocompatibility of the nanoparticles in the systemic circulation. The produced nanoparticles were further functionalized by hyaluronic acid (HA), through the modification of the nanoparticles with HA conjugated PDA, to specifically target CD44 overexpressing tumour cells. The results showed that the nanoparticles accumulated significantly at the tumour site and achieved photoacoustic imaging-guided combinational chemo-/photothermal therapy with high therapeutic efficacy (Fig. 17).

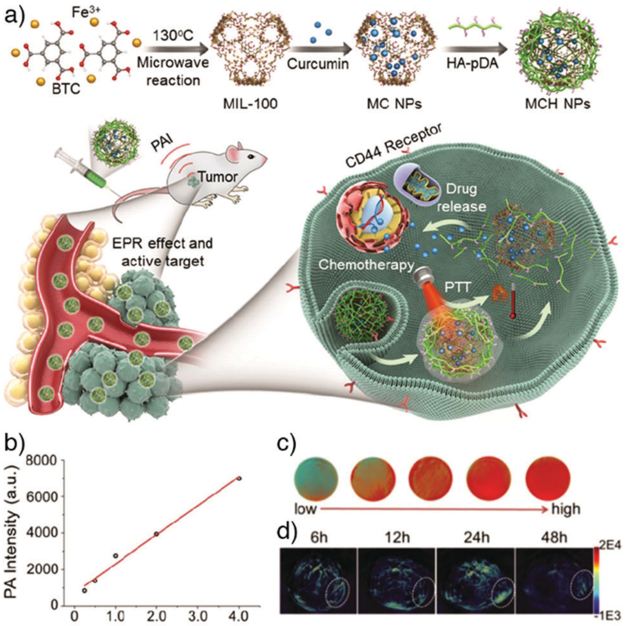

Fig. 17 (a) Schematic illustration for the construction and applications of MIL-100(Fe) for photoacoustic imaging-guided chemo-/photothermal combinational tumour therapy. (b) PA intensity of the nanoparticles at different concentrations. (c) Corresponding *in vitro* PA images. (d) PA images of HeLa tumour-bearing mice at different time points after intravenous injection with the nanoparticles. Reproduced with permission.[20] Copyright (2018) American Chemical Society.

Yang *et al.* reported the synthesis of ZIF-8 derived carbon nanoparticles (ZCNs) using a one-step procedure, to achieve PAI-guided cancer phototherapy and to investigate the effects of the nanoparticle size on phototherapy and PAI contrast ability.[35] The ZCNs acted as photothermal agents and photosensitizers by simultaneously generating heat and reactive oxygen species which caused efficient tumour ablation upon NIR laser irradiation, as monitored by *in vivo* PAI. Furthermore, the results showed that the increase in the nanoparticle size provided enhanced phototherapy effects and PA signal intensity (Fig. 18).

Similarly, Zhang *et al.* demonstrated new nanosized metal–organic particles constructed directly using an organic dye, tetrahydroxyanthraquinone (THQ), as linker connected by Cu(II) ions serving as dual-mode therapeutics for PAI-guided photothermal/chemotherapy in the NIR II window (from 1000 to 1350 nm of the optical spectrum).[160] After PEGylation, the nanoparticles (termed Cu-THQNPs) achieved excellent biocompatibility and colloidal stability. Their strong absorption in the NIR II window and photo-induced electron transfer (PET) mechanism enabled Cu-THQNPs to act as excellent photothermal agents with a high light-to-heat conversion efficiency (51.3%) at 1064 nm, and also as excellent photoacoustic contrast agents. Moreover, the degradation of the nanoparticles by tumour specific acidic cleavage of the coordination bonds caused the release of Cu(II) into the tumour area, enhancing antitumour activity through catalysing conversion of hydrogen peroxide (H_2O_2) to hydroxyl radicals ($^{\bullet}OH$). In another study, ZIF-8 nanoparticles were combined with AuNRs to obtain PA contrast agents (AuNR@ZIF-8) with high PAI capacity and biocompatibility.[161] AuNR@ZIF-8 core–shell nanocomposites were successfully built through a facile step-by-step synthesis method, which involves attaching PVP to the surface of the AuNR core and subsequently growth of ZIF-8 on the AuNR surface. The resulting AuNR@ZIF-8 nanoparticles demonstrated high NIR absorption, good photothermal conversion and PAI efficiency owing to the AuNR core, and easy modification of the MOF surface, as well as high biocompatibility.

Overall, MOFs are being widely investigated as highly promising imaging agents for a number of diverse techniques, primarily as a consequence of their synthetic versatility and the possibility of combining imaging with drug delivery. Imaging functionality can be intrinsic structural components of the MOF or guests bound within pores or on particle surface, and can be incorporated during synthesis or postsynthetically, while MOFs can easily be hybridised with a range of other nanomaterials. It is this versatility that means multiple imaging functionalities can also easily be installed in single particles, leading to multimodal imaging agents.

3. MOFs as multimodal imaging agents

Integration of multiple imaging modalities within a single material is a highly promising approach to overcome the

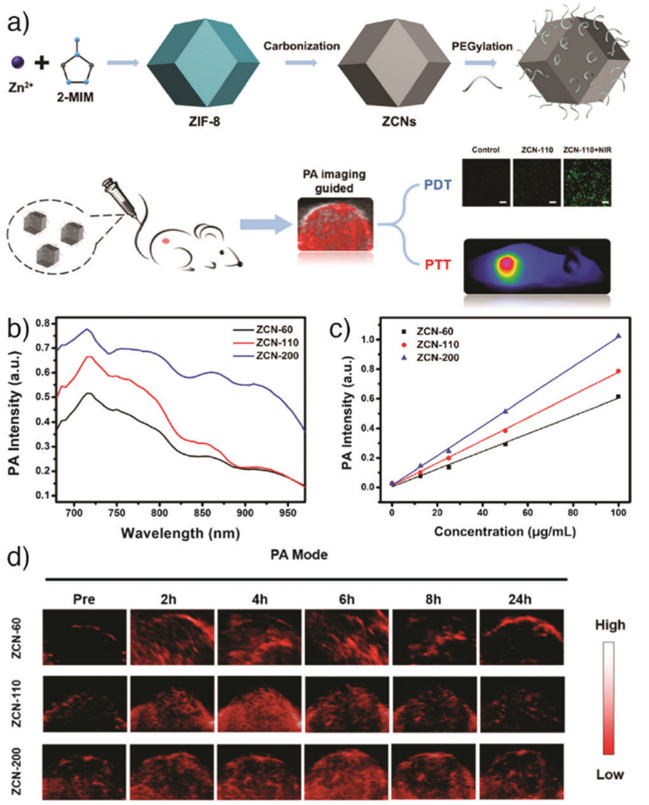

Fig. 18 (a) Schematic representation of the synthesis and applications of ZIF-8-derived carbon nanoparticles (ZCNs) for PAI-guided photothermal/photodynamic combined therapy. PA signal intensity of ZCNs *in vitro* at (b) different excitation wavelengths, and (c) various concentrations. (d) PA imaging of A549 tumour-bearing mice at different times after intravenous injection with ZCNs. The images display the tumour region of the mice. Reproduced with permission.[35] Copyright (2018) American Chemical Society.

limitations of existing imaging techniques and obtain imaging agents with high stability, biocompatibility, enhanced imaging sensitivity and resolution capacity. The structural and compositional diversity of NMOFs, combined with the wide range of potential functionalization and hybridisation protocols available, means they are excellent candidates for multimodal imaging, in some cases in combination with therapeutic applications.

3.1. OI/MRI

Combination of optical and MR imaging features within MOF nanoparticles is one of the most applied strategies to achieve non-invasive bimodal imaging agents with superior contrast capacity. Kundu *et al.* reported the application of two porous gadolinium(III)-based MOFs, Gd–pDBI-1 and Gd–pDBI-2 (pDBI = 1,4-bis(5-carboxy-1*H*-benzimidazole-2-yl)benzene) for bimodal imaging (Fig. 19a).[162] The change in metal precursor from $Gd(NO_3)_3{\cdot}6H_2O$ to $Gd(OAc)_3{\cdot}6H_2O$ induced the formation of two different MOFs, Gd–pDBI-1 and Gd–pDBI-2, respectively (Fig. 19b), where enhanced porosity was reflected in the higher BET surface area for Gd–pDBI-2 (614 $m^2\ g^{-1}$) compared to the negligible N_2 adsorption by Gd–pDBI-1 (33 $m^2\ g^{-1}$, Fig. 19c). The images recorded by SEM exhibited uniformly shaped spindle-like particles about 1 mm in length and 0.3 mm in width at the centre of Gd–pDBI-2, whereas Gd–pDBI-1 displayed extensively aggregated, 120 nm rod-shaped particles (Fig. 19a). The fluorescent pDBI linker in the structure enabled the application of the MOFs as fluorescent agents – Gd–pDBI-2 exhibited greater luminescence than Gd–pDBI-1 (Fig. 19d) – while the Gd core led them to serve as MRI contrast agents. Confocal microscopy images revealed the bright blue-coloured fluorescence of Gd–pDBI-2 within the cytoplasm of the MCF-7 cells at an excitation wavelength of 405 nm *in vitro* (Fig. 19e–g). Of the two MOFs, Gd–pDBI-2 exhibited higher longitudinal relaxivity (r_1) as an MRI contrast agent (Fig. 19h and i). *In vivo* MR images conducted on a mouse model confirmed the MRI capabilities of Gd–pDBI-2 particles, generating a partial white contrast on the spleen, kidney, and liver of the animal by using a 0.3 T clinical MRI scanner, as shown in Fig. 19j and k.

In another example, Gao *et al.* reported the synthesis of multifunctional MOFs for fluorescence/magnetic resonance dual-mode imaging and targeted drug delivery.[44] In the study, MIL-53(Fe)-NH_2 NMOFs, which have attractive properties such as well-defined pores and intense magnetism, were loaded with the anticancer drug 5-FU and decorated with FA for tumour targeting. The nanoparticles were further functionalized by conjugation of a fluorescent reagent, 5-carboxylfluorescein (5-FAM), and employed successfully as MR and optical imaging agents with a satisfactory magnetic performance and strong green fluorescence emission. In addition, the particles achieved higher cellular uptake and inhibition of cell growth in FA-positive MGC-803 cells compared with FA-negative HASMC cells. The group alternatively showed *in situ* growth of MOFs on the surface of other MOFs as a new strategy to construct dual imaging materials combining MR and optical imaging properties in the same entity.[163] Rodlike Eu-MOFs of formula $[Eu(BTC)(H_2O)]_n$, which emit red fluorescence, were grown on the surface of spherical MIL-100(Fe) particles that could act as MRI contrast agents, by a simple *in situ* growth method. MIL-100(Fe) particles were suspended in a DMF/water solution of $Eu(NO)_3{\cdot}6H_2O$ and sodium acetate at 60 °C for 72 h, with growth of the Eu-MOF presumably a consequence of partial dissolution at MIL-100(Fe) surfaces and release of BTC linkers. The Fe-MOF/Eu-MOF heterostructures simultaneously exhibited red fluorescence arising from the Eu-MOF, and enhanced T_2-weighted MR images from MIL-100(Fe) acting as a contrast agent. The nanocomposites showed strong fluorescence in HASMC human aortic smooth muscle cells and MGC-803 cancer cells, as well as *in vivo* in athymic nude mice. The Fe-MOF/Eu-MOF heterostructures were further loaded with 5-FU and employed as a therapeutic agent with strong cell growth inhibitory effect in MGC-803 cells.

Li *et al.* reported the integration of rare-earth-doped UCNPs with MOFs to obtain core–shell UCNP@MOF for luminescent/magnetic dual-mode targeted imaging.[164] The particles were prepared by the combination of single $NaYF_4$:Yb,Er UCNP core particles with a MIL-101(Fe)-NH_2 NMOF shell, followed by conjugation of poly(ethylene glycol)-2-amino ethyl ether acetic

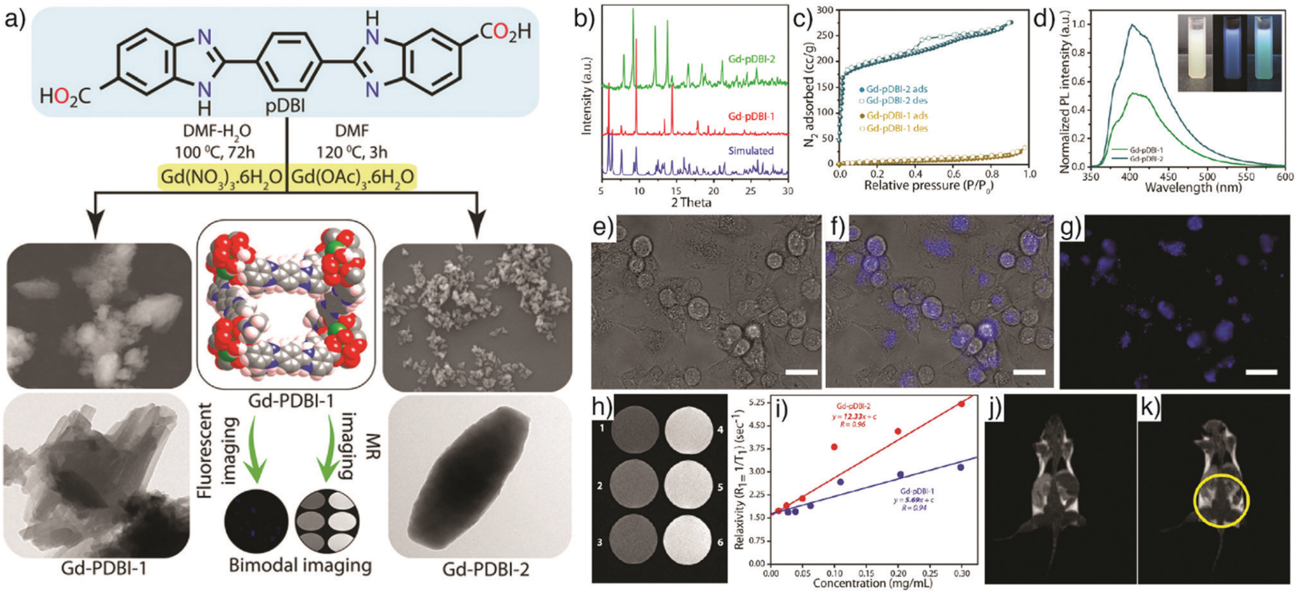

Fig. 19 (a) Schematic illustration of the synthesis of Gd–pDBI-1 and Gd–pDBI-2 from the luminescent linker pDBI under different reaction conditions and their applications for simultaneous fluorescence and MR imaging. Left panel displays SEM (top) and TEM (bottom) images of Gd–pDBI-1; right panel displays SEM (top) and TEM (bottom) images of Gd–pDBI-2. (b) PXRD patterns, (c) N_2 adsorption isotherms, and (d) PL spectra of Gd–pDBI-1 and Gd–pDBI-2; inset represents aqueous dispersion of Gd–pDBI-2 under visible light (white), 365 nm UV light (blue), and 254 nm UV light (bluish green). Confocal microscopic images of MCF-7 cells incubated with Gd–pDBI-2: (e) bright-field, (f) merged, and (g) fluorescence image (λ_{ex} = 405 nm). Scale bars 20 μm. (h) T_1-Weighted phantom image of Gd–pDBI-2 at different Gd(III) concentrations (1: 12.5 μg mL^{-1}, 2: 25 μg mL^{-1}, 3: 50 μg mL^{-1}, 4: 100 μg mL^{-1}, 5: 200 μg mL^{-1}, 6: 300 μg mL^{-1}). (i) Comparison of longitudinal relaxivity (r_1) of Gd–pDBI-1 and Gd–pDBI-2. *In vivo* MR images of (j) control mouse and (k) mouse injected with Gd–pDBI-2. Reproduced with permission.[162] Copyright (2016) Wiley-VCH Verlag GmbH & Co. KGaA, Weinheim.

acid (NH_2–PEG–COOH) and FA tumour targeting unit, which yielded PEGylated core–shell UCNP@MIL-101(Fe)-NH_2@PEG–FA nanostructures. Luminescence from the UCNPs is clearly visible (Fig. 20a) and the Fe-MOF acted as a T_2-weighted MRI contrast agent (Fig. 20b). *In vitro* studies (Fig. 20c) performed on KB cells (FR-positive) and MCF-7 cells (FR-negative), and *in vivo* studies conducted on KB-tumour bearing mice (Fig. 20d–i), demonstrated that the core–shell nanostructures can simultaneously function as tumour targeted dual-mode UCL/MR imaging agents, providing high luminescence intensity from the UCNP core, and T_2-MRI properties as the MIL-101(Fe)-NH_2 shell achieves a distinct darkening effect, therefore enabling sensitive imaging with low toxicity and high uptake in FR-positive KB cells.

In addition to their T_2-MR imaging properties, SPIONs have also attracted great attention for their photothermal conversion efficiency. Zhang *et al.* combined these characteristics with the photodynamic therapy and fluorescence imaging abilities of a porphyrin MOF structure by constructing core–shell magnetic porphyrin MOF nanocomposites for fluorescence-MR dual-modality imaging-guided photothermal and photodynamic dual-therapy.[45] The core–shell nanocomposites were fabricated by the encapsulation of Fe_3O_4 nanoparticle clusters in a carbon shell, and then *in situ* self-assembly of a porphyrin MOF (PMOF), constructed from Zr ions and TCPP with the PCN-223 structure, on the surface of these Fe_3O_4@C nanoparticles. The Fe_3O_4@C nanoparticles served as T_2-weighted MR imaging and PTT agents, while the PMOF enabled simultaneous fluorescence imaging and PDT in the nanocomposite structure. The resulting Fe_3O_4@C@PMOF nanocomposites demonstrated high biocompatibility and stability, and effective fluorescence and MR dual-modality imaging with high accumulation in the tumour site of tumour-bearing mice. The nanostructures also achieved effective photothermal and photodynamic therapy of tumours without damaging normal tissues through the controllable and local irradiation of the laser.

3.2. MRI/CT

Boyes and co-workers showed utilization of NMOFs as MR and CT bimodal imaging agents by combining $[Gd(BDC)_{1.5}(H_2O)_2]_n$ nanorods, constructed from Gd(III) magnetic centres connected by BDC linkers, and CTAB to prevent the aggregation of the nanoparticles, with Au NPs *via* poly(acrylic acid) (PAA) bridges. The highly stable Gd-MOF–PAA–Au nanocomposites showed excellent MRI contrast with higher longitudinal relaxivity than the clinically used MRI positive contrast agent Magnevist through Gd(III) in the structure, and strong CT contrast through Au NPs providing a source of high-*Z* elements. The composites, however, were not tested towards any biological materials.[165]

3.3. MRI/PAI

Chen *et al.* described a facile approach to synthesize polypyrrole (PPy) composite materials (PPy@MOFs), where a PPY core was surrounded by a MIL-100(Fe) shell loaded with DOX, for magnetic resonance/photoacoustic dual-mode imaging combined with chemo-photothermal cancer therapy.[166] PPy NPs are well known for their high photothermal conversion efficiency that allows efficient photothermal cancer therapy,

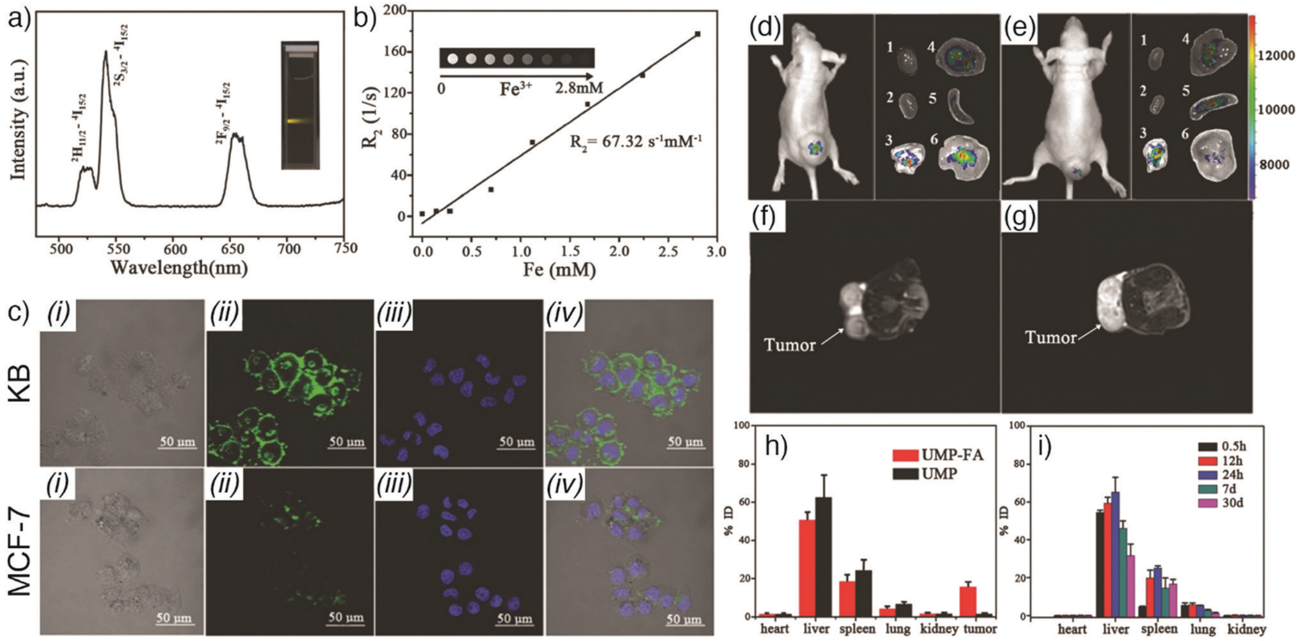

Fig. 20 (a) Upconversion emission spectra of UCNP@MIL-101(Fe)-NH$_2$@PEG–FA nanostructures (inset shows UCNP@MIL-101(Fe)-NH$_2$@PEG–FA dispersed in water under 980 nm diode excitation). (b) Relaxation rate r_2 ($1/T_2$) *versus* concentrations of UCNP@MIL-101(Fe)-NH$_2$@PEG–FA at room temperature measured by 3T MRI scanner (inset shows T_2-weighted MR images of the nanostructures with various concentrations). (c) CLSM images of KB (top) and MCF-7 (bottom) cells incubated with UCNP@MIL-101(Fe)-NH$_2$@PEG-FA: (i) bright field, (ii) green channel images collected at 500–560 nm, (iii) cell nucleus stained with Hoechst 33342 (blue fluorescence), and (iv) merged images. Dual-modal UCL/MR *in vivo* imaging of KB tumour-bearing mice and their dissected organs at 24 h post-injection of (d) UCNP@MIL-101(Fe)-NH$_2$@PEG–FA (UMP-FA, targeted) and (e) UCNP@MIL-101(Fe)-NH$_2$@PEG (UMP, without FA, non-targeted). (1) Heart; (2) kidney; (3) lung; (4) liver; (5) spleen; (6) KB tumour. T_2-MRI images of KB tumour-bearing mice at 24 h after intravenous injection with (f) UCNP@MIL-101(Fe)-NH$_2$@PEG–FA and (g) UCNP@MIL-101(Fe)-NH$_2$@PEG. (h) Corresponding biodistributions of the two samples. (i) Biodistribution of UCNP@MIL-101(Fe)-NH$_2$@PEG after 0.5 h, 12 h, 24 h, 7 d, and 30 d following intravenous injection. Reproduced with permission.[164] Copyright (2015) Wiley-VCH Verlag GmbH & Co. KGaA, Weinheim.

and strong optical contrast for PAI.[167–170] To obtain PPy@MOFs, pyrrole was reacted with PVP and $FeCl_3$ in deionized water to generate the PPy core, where PVP was utilized as a stabilizing agent and $FeCl_3$ as a catalyst. Then, trimesic acid was reacted with Fe(III) ions on the PPy surface, which act as reactive sites, for the construction of PPy@MIL-100(Fe), and finally the nanocomposites were loaded with DOX. PPy@MOFs exhibited good biocompatibility and dual-mode PA and MR imaging, as well as excellent photothermal conversion efficiency (~40%) and NIR/pH-triggered release of DOX, resulting in a synergistic chemo-photothermal therapy of HepG2 human hepatocellular carcinoma cells.

3.4. OI/MRI/PAI

MOFs have also been employed as contrast agents for triple-modality OI/MRI/PAI, especially for early diagnosis of tumours. For example, Cai *et al.* reported NMOF-based multimodal imaging guided photothermal cancer therapy.[43] MIL-100(Fe), as a T_2-weighted MRI agent, was combined with a photo-responsive NIR emitting organic dye indocyanine green (ICG), after conjugation of the MOFs with hyaluronic acid (HA). The produced nanoparticles (MOF@HA@ICG NPs, Fig. 21a) showed high loading content of ICG (40%), and strong NIR emission intensity and photostability. The *in vitro* (Fig. 21b–e) and *in vivo* (Fig. 21f–j) imaging and photothermal toxicity studies exhibited enhanced cellular uptake and tumour accumulation of the HA-functionalized nanoparticles in CD44-positive MCF-7 cells and MCF-7 tumour-bearing mice, providing an effective photothermal toxicity, as well as strong fluorescence, photoacoustic, and magnetic resonance multi-modal imaging capacities compared to MOF@ICG NPs (non-HA-targeted) and free ICG.

Similarly, Yang *et al.* showed the synthesis of MIL-53(Fe) loaded with a NIR cyanine dye (cypate), which can interact with Fe(III) to construct precursor complexes, for near-infrared fluorescence (NIRF), MR and PA imaging guided PTT/PDT *in vivo*.[171] The cyanine dye in the composition provided NIRF and PA imaging abilities, and acted jointly as a PTT and PDT agent by transforming NIR laser to heat and generating ROS under NIR irradiation, respectively, while MIL-53(Fe) enabled MR imaging. Moreover, incorporation of cypate molecules into the structure increased the extent of defects in the MOF nanoparticles, which enhanced the aqueous solubility and bioavailability of cypate. Further modification of the particles with transferrin, which has high binding affinity for the transferrin receptors overexpressed on cancer cells, improved internalization of the nanoparticles in A549 cells and in tumour regions of A549 tumour-bearing mice with higher NIRF and PA intensity, and more effective tumour ablation was observed compared to untargeted nanoparticles upon a low power laser.

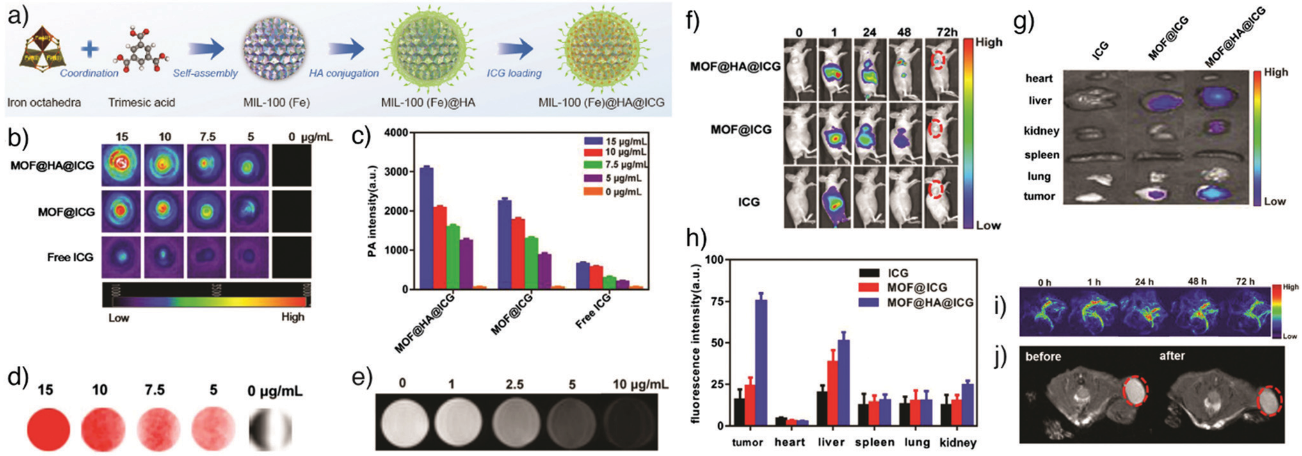

Fig. 21 (a) Schematic illustration of the synthesis of MIL-100(Fe) NPs and their functionalization by HA conjugation and ICG loading. Imaging of MCF-7 cells *in vitro*: (b) PA images with (c) associated PA intensities for free ICQ, ICQ@MIL-100(Fe), and ICQ@HA@MIL-100(Fe), (d) fluorescence images and (e) T_2-weighted MR images of MCF-7 cells after incubation with ICQ@HA@MIL-100(Fe). Imaging of MCF-7 tumour-bearing mice *in vivo*: (f) fluorescence images of mice injected with free ICQ, ICQ@MIL-100(Fe), and ICQ@HA@MIL-100(Fe) solutions, (g) corresponding *ex vivo* fluorescence images, (h) fluorescence intensities of the organs and tumours, (i) *in vivo* PA and (j) T_2-weighted MR images after MOF@HA@ICG treatment. Reproduced with permission.[43] Copyright (2016) American Chemical Society.

3.5. MRI/CT/PAI

MOF nanoparticles have also been used as triple-modality MRI/CT/PAI contrast agents by fabricating Au@MIL-88A(Fe) nanostructures *via* controllable growth of a MIL-88A(Fe) shell layer on the surface of AuNRs.[172] The core–shell Au@MIL-88(Fe) nanocomposites were further modified by poly(ethylene glycol)–carboxylic acid (PEG–COOH) for higher colloidal stability *in vivo*. The AuNR core in the structure provided CT enhancement and PAI optical properties simultaneously, while MIL-88(Fe) served as T_2-weighted MRI contrast agent. The prepared nanostructures showed low toxicity, and enabled high spatial resolution and effective contrast during *in vivo* MRI, CT and PAI imaging of glioma. In another study, Yang *et al.* showed the construction of core–shell and co-doped Mn/Hf-IR825@PDA–PEG NMOPs (NMOP-PEG) through a post-synthesis cation exchange method, and described their application as MRI and PAI contrast agents for bimodal imaging, and as radiosensitizers and photothermal agents for synergistic thermo-radiotherapy.[159] The particles were produced by mixing the NMOPs (nanoscale metal–organic particles) containing Mn(II) and IR825, a NIR dye, with Hf(IV), and coating with polydopamine (PDA) and further conjugation with PEG. The Mn(II) ions served as a contrast agent for T_1-weighted MR imaging, IR825 provided strong PA contrast and a photothermal effect due to high NIR absorption, Hf(IV) enabled the utilization of the particles as CT contrast agents and for radiation therapy with strong X-ray absorbance, and the further coatings by PDA and PEG endowed them with excellent colloidal stability. The as-synthesized Mn/Hf-IR825@PDA–PEG NMOPs showed efficient tumour retention ability after intravenous injection in a mouse tumour model, which was confirmed by MR/CT and PA images. Additionally, they demonstrated efficient tumour killing efficacy by synergistic PTT and radiation therapy (RT) treatment, which is attributed to the increased oxygenation in the tumour region induced by PTT that repress tumour hypoxia-related RT resistance, and radio-sensitization induced by Hf. Furthermore, the particles were almost completely excreted from the mouse body without causing any dark toxicity within a month, showing them to be biodegradable and multifunctional nanoplatforms for highly integrated clinical functions.

4. Conclusions and perspectives

In this review, we have highlighted and discussed the use of MOFs and their composites as promising imaging agents for various imaging modalities in clinical applications. Table 1 summarizes the applications of selected NMOFs as bioimaging agents based on all imaging strategies and examples explained above. For bioimaging, MOFs offer a variety of advantages such as tunable porosity, controlled structure, synthetic versatilities, diverse sizes and morphologies, high surface area, and easy functionalization, which allows one to endow them with multiple functionalities and properties. The wide-ranging choice of both metal ions as coordination centres and organic ligands as linkers further contribute to their compositional and structural diversities. Their porous structures and high surface area allow them to be simultaneously loaded with a wide variety of therapeutic and imaging structures in large amounts, creating MOF-based multimodal imaging-guided theranostic systems. The tunable surface chemistry provides a facile route to modification with various molecules to enhance their biocompatibility, stability in physiological media, and/or the ability to targeting to a specific region in the body. Biodegradability of NMOFs, combined with rapid excretion and short-term body retention, provide a potential pathway to their safe utilization for *in vivo* applications.

Beside being conjugated or loaded with active molecules, NMOFs can also be directly constructed from various intrinsically active metal ions or linkers. The use of certain inorganic metal ions with imaging contrast abilities, *e.g.* Fe(III), Mn(II), Gd(III) and

Table 1 A summary of selected NMOFs for bioimaging applications

MOFs	Imaging agent	Drug/cargo	Imaging strategy	Further applications	Ref.
Rs⊂nMOF-801, R6G⊂nUiO-67	Resorufin, rhodamine-6G	—	OI	Liver cell targeting *via* galactosylation	18
MIL-53(Al)-NH_2	RhB	TCH, 5-FU	OI	Drug loading and release	29
RhB/ZIF-90	RhB	—	OI	Mitochondrial ATP imaging	81
MIL-101(Fe)	Br-BODIPY	ESCP	OI	Drug loading and release	59
Zr-based MOFs	Calcein	α-Cyano-4-hydroxycinnamic acid	OI	Drug delivery, endocytosis	64
cal-TPP@(DCA_5-UiO-66)	Calcein	DCA, TPP	OI	Mitochondria-targeted drug delivery	69
AuNR@MOFs@CPT	TCPP	CPT, Au NRs	OI	PDT/PTT/chemotherapy	80
NH_2-MIL-101(Fe)	Chlorine e6	CPT	OI	PDT/chemotherapy, tumour targeting *via* FA, intracellular CaB targeting *via* CaB substrate	91
DOX@Mi-UiO-68-FA	DOX	DOX	OI	Tumour targeting and therapy	66
FA@Eu:TMU-62-NH_2	Eu	5-FU	OI	pH-Responsive targeted drug delivery	103
$NaLnF_4$@MOF-Ln	Ln = Y, Tm, Yb, Eu	DOX	OI (dual-mode luminescence)	pH-Responsive drug delivery	105
ZGGO@ZIF-8-DOX	ZGGO PLNPs	DOX	OI (persistent luminescence)	pH-Responsive drug delivery	74
UCNP@ZIF-8/FA	$NaYF_4$:Yb(III), Er(III)	5-FU	OI (UCL)	pH-Responsive targeted drug delivery	76
C-dot@ZIF-8	C-dots	5-FU	OI	pH-Responsive drug delivery	79
(nUiO-67)-$[Ru(bpy)_3]^{2+}$	$[Ru(bpy)_3]^{2+}$		OI (two-photon fluorescence)	Photodynamic therapy	119
Gd-Based MOFs	Gd(III)	Eu(III), Tb(III)	T_1-Weighted MRI	Luminescence imaging	28
Eu,Gd-NMOF@SiO_2	Gd(III)	Eu(III)	T_1- and T_2-weighted MRI	Luminescence imaging, tumour targeting *via* c(RGDyK)	19
Mn-IR825@PDA–PEG	Mn(II)	IR825	T_1-Weighted MRI	Photothermal therapy	141
Mn- and Gd-based MOFs	Gd(III), Mn(II)	—	T_1-Weighted MRI	—	142
Iron(III) carboxylate MOFs (MIL-53, MIL-88A, MIL-88Bt, MIL-89, MIL-100 and MIL-101_NH_2)	Fe(III)	Busulfan, azidothymidine triphosphate, DOX or cidofovir	T_2-Weighted MRI	Chemotherapy	31
DOX@ZIF-HA	Fe(III)	DOX	T_1-Weighted MRI	Prostate cancer targeting *via* HA, chemotherapy	144
Fe_3O_4@UiO-66	Fe_3O_4	DOX	T_2-Weighted MRI	Chemotherapy	136
Fe_3O_4@IRMOF-3/FA	Fe_3O_4	PTX, RITC	T_2-Weighted MRI	Chemotherapy, fluorescence imaging	145
UiO-PDT	BODIPY	—	CT	—	33
^{89}Zr–UiO-66/Py-PGA–PEG-F3	^{89}Zr(IV)	DOX, Py–PGA–PEG	PET	Tumour targeting *via* F3 peptide, chemotherapy, fluorescence imaging	34
HA–PDA coated MIL-100(Fe)	Fe(III)	Curcumin	PAI	Chemotherapy, PTT, cancer targeting *via* HA	20
ZIF-8-derived carbon nanoparticles	Carbon		PAI	PDT, PTT	35
Gd–pDBI-1 and Gd–pDBI-2	Gd(III)/pDBI	—	T_1-Weighted MRI/OI	—	162
MIL-53(Fe)-NH_2-FA-5-FAM/5-FU	Fe(III)/5-FAM	5-FU	T_2-Weighted MRI/OI	Tumour targeting *via* FA, chemotherapy	44
PPy@MIL-100(Fe)	Fe(III)/PPy	DOX	T_2-Weighted MRI/PAI	NIR/pH-triggered drug release, chemotherapy, PTT	166
MOF@HA@ICG NPs	Fe(III)/ICG	—	T_2-Weighted MRI/OI/PAI	PTT, tumour targeting *via* HA	43
Mn/Hf-IR825@PDA-PEG	Mn(II)/IR825/Hf(IV)	—	T_1-Weighted MRI/PAI/CT	Thermo-radiotherapy	159

Hf(IV), enables the construction of MOFs as contrast agents for OI, MRI, CT, PET or PAI. Additionally, by using organic linkers with imaging capabilities, such as luminescent porphyrin derivatives, simultaneous imaging and therapy can be achieved. However, there are still many important limitations and challenges that need to be optimized for potential clinical applications of MOFs as imaging contrast agents. Firstly, a systematic *in vivo* toxicity evaluation, considering the accumulation, retention, and metabolism of any residuals, is essential. This would also require that any MOF proposed as an imaging device could be synthesised with highly reproducible physical properties such as particle size, morphology, and surface chemistry; precision manufacture at this level is not trivial. Secondly, the poor solubility and colloidal stability of MOFs in body fluids significantly limit their *in vivo* bioimaging applications. For instance, many Zn-carboxylate MOFs exhibit low stability in aqueous conditions due to the labile Zn carboxylate coordination. On the other hand, Zr-based MOFs, which are typically chemically inert, have high affinity towards phosphate ions found in culture medium and phosphate-buffered saline.[173] As such, the degradation mechanism and biostability of currently available MOFs requires further studies. However, these problems can potentially be solved by selecting low-toxicity metal ions and organic linkers, and by appropriate functionalization and/or coating of MOFs. Their synthetic, compositional, and functional diversities mean that highly complex systems can be assembled relatively easily, and so it is expected that they will play a significant role in the biomedical field in the near future.

Conflicts of interest

The authors declare no conflict of interest.

Acknowledgements

RSF thanks the Royal Society for a University Research Fellowship and the University of Glasgow for funding. This project received financial support in part from the European Research Council (ERC) under the European Union's Horizon 2020 Programme for Research and Innovation (grant agreement no. 677289, SCoTMOF, ERC-2015-STG).

References

1 Y. Sun, L. Zheng, Y. Yang, X. Qian, T. Fu, X. Li, Z. Yang, H. Yan, C. Cui and W. Tan, *Nano-Micro Lett.*, 2020, **12**, 1–29.
2 X. L. Wang, C. Qin, S. X. Wu, K. Z. Shao, Y. Q. Lan, S. Wang, D. X. Zhu, Z. M. Su and E. B. Wang, *Angew. Chem., Int. Ed.*, 2009, **48**, 5291–5295.
3 H.-C. Zhou and S. Kitagawa, *Chem. Soc. Rev.*, 2014, **43**, 5415–5418.
4 A. R. Millward and O. M. Yaghi, *J. Am. Chem. Soc.*, 2005, **127**, 17998–17999.
5 M. Eddaoudi, J. Kim, N. Rosi, D. Vodak, J. Wachter, M. O'Keeffe and O. M. Yaghi, *Science*, 2002, **295**, 469–472.
6 J. Lee, O. K. Farha, J. Roberts, K. A. Scheidt, S. T. Nguyen and J. T. Hupp, *Chem. Soc. Rev.*, 2009, **38**, 1450–1459.
7 J. S. Seo, D. Whang, H. Lee, S. Im Jun, J. Oh, Y. J. Jeon and K. Kim, *Nature*, 2000, **404**, 982–986.
8 C. Wang, T. Zhang and W. Lin, *Chem. Rev.*, 2012, **112**, 1084–1104.
9 P. Serra-Crespo, M. A. Van Der Veen, E. Gobechiya, K. Houthoofd, Y. Filinchuk, C. E. Kirschhock, J. A. Martens, B. F. Sels, D. E. De Vos and F. Kapteijn, *J. Am. Chem. Soc.*, 2012, **134**, 8314–8317.
10 L. E. Kreno, K. Leong, O. K. Farha, M. Allendorf, R. P. Van Duyne and J. T. Hupp, *Chem. Rev.*, 2012, **112**, 1105–1125.
11 Z. Hu, B. J. Deibert and J. Li, *Chem. Soc. Rev.*, 2014, **43**, 5815–5840.
12 W. Yang, J. Feng, S. Song and H. Zhang, *ChemPhysChem*, 2012, **13**, 2734–2738.
13 H. Zheng, Y. Zhang, L. Liu, W. Wan, P. Guo, A. M. Nyström and X. Zou, *J. Am. Chem. Soc.*, 2016, **138**, 962–968.
14 S. Beg, M. Rahman, A. Jain, S. Saini, P. Midoux, C. Pichon, F. J. Ahmad and S. Akhter, *Drug Discovery Today*, 2017, **22**, 625–637.
15 I. Abánades Lázaro, C. J. Wells and R. S. Forgan, *Angew. Chem., Int. Ed.*, 2020, **59**, 5211–5217.
16 M. D. Allendorf, C. A. Bauer, R. Bhakta and R. Houk, *Chem. Soc. Rev.*, 2009, **38**, 1330–1352.
17 D. Liu, R. C. Huxford and W. Lin, *Angew. Chem., Int. Ed.*, 2011, **50**, 3696–3700.
18 U. Ryu, J. Yoo, W. Kwon and K. M. Choi, *Inorg. Chem.*, 2017, **56**, 12859–12865.
19 G. D. Wang, H. Chen, W. Tang, D. Lee and J. Xie, *Tomography*, 2016, **2**, 179–187.
20 Y. Zhang, L. Wang, L. Liu, L. Lin, F. Liu, Z. Xie, H. Tian and X. Chen, *ACS Appl. Mater. Interfaces*, 2018, **10**, 41035–41045.
21 K. M. Taylor, W. J. Rieter and W. Lin, *J. Am. Chem. Soc.*, 2008, **130**, 14358–14359.
22 W. Hatakeyama, T. J. Sanchez, M. D. Rowe, N. J. Serkova, M. W. Liberatore and S. G. Boyes, *ACS Appl. Mater. Interfaces*, 2011, **3**, 1502–1510.
23 A. Foucault-Collet, K. A. Gogick, K. A. White, S. Villette, A. Pallier, G. Collet, C. Kieda, T. Li, S. J. Geib and N. L. Rosi, *Proc. Natl. Acad. Sci. U. S. A.*, 2013, **110**, 17199–17204.
24 L. Chen, J.-W. Ye, H.-P. Wang, M. Pan, S.-Y. Yin, Z.-W. Wei, L.-Y. Zhang, K. Wu, Y.-N. Fan and C.-Y. Su, *Nat. Commun.*, 2017, **8**, 15985.
25 M. X. Wu and Y. W. Yang, *Adv. Mater.*, 2017, **29**, 1606134.
26 A. C. McKinlay, R. E. Morris, P. Horcajada, G. Férey, R. Gref, P. Couvreur and C. Serre, *Angew. Chem., Int. Ed.*, 2010, **49**, 6260–6266.
27 J. Yang and Y. W. Yang, *Small*, 2020, **16**, 1906846.
28 W. J. Rieter, K. M. Taylor, H. An, W. Lin and W. Lin, *J. Am. Chem. Soc.*, 2006, **128**, 9024–9025.
29 X. Gao, Y. Wang, G. Ji, R. Cui and Z. Liu, *CrystEngComm*, 2018, **20**, 1087–1093.
30 K. M. Park, H. Kim, J. Murray, J. Koo and K. Kim, *Supramol. Chem.*, 2017, **29**, 441–445.
31 P. Horcajada, T. Chalati, C. Serre, B. Gillet, C. Sebrie, T. Baati, J. F. Eubank, D. Heurtaux, P. Clayette and C. Kreuz, *Nat. Mater.*, 2010, **9**, 172–178.
32 Y. Zhang, C. Liu, F. Wang, Z. Liu, J. Ren and X. Qu, *Chem. Commun.*, 2017, **53**, 1840–1843.
33 T. Zhang, L. Wang, C. Ma, W. Wang, J. Ding, S. Liu, X. Zhang and Z. Xie, *J. Mater. Chem. B*, 2017, **5**, 2330–2336.
34 D. Chen, D. Yang, C. A. Dougherty, W. Lu, H. Wu, X. He, T. Cai, M. E. Van Dort, B. D. Ross and H. Hong, *ACS Nano*, 2017, **11**, 4315–4327.
35 P. Yang, Y. Tian, Y. Men, R. Guo, H. Peng, Q. Jiang and W. Yang, *ACS Appl. Mater. Interfaces*, 2018, **10**, 42039–42049.
36 J. Della Rocca, D. Liu and W. Lin, *Acc. Chem. Res.*, 2011, **44**, 957–968.
37 C. He, D. Liu and W. Lin, *Chem. Rev.*, 2015, **115**, 11079–11108.

38 D. Liu, K. Lu, C. Poon and W. Lin, *Inorg. Chem.*, 2014, **53**, 1916–1924.

39 Y. Guari, J. Larionova, M. Corti, A. Lascialfari, M. Marinone, G. Poletti, K. Molvinger and C. Guérin, *Dalton Trans.*, 2008, 3658–3660.

40 K. M. Taylor, A. Jin and W. Lin, *Angew. Chem., Int. Ed.*, 2008, **47**, 7722–7725.

41 J.-L. Bridot, A.-C. Faure, S. Laurent, C. Rivière, C. Billotey, B. Hiba, M. Janier, V. Josserand, J.-L. Coll, L. Vander Elst, R. Muller, S. Roux, P. Perriat and O. Tillement, *J. Am. Chem. Soc.*, 2007, **129**, 5076–5084.

42 K. E. Dekrafft, W. S. Boyle, L. M. Burk, O. Z. Zhou and W. Lin, *J. Mater. Chem.*, 2012, **22**, 18139–18144.

43 W. Cai, H. Gao, C. Chu, X. Wang, J. Wang, P. Zhang, G. Lin, W. Li, G. Liu and X. Chen, *ACS Appl. Mater. Interfaces*, 2017, **9**, 2040–2051.

44 X. Gao, M. Zhai, W. Guan, J. Liu, Z. Liu and A. Damirin, *ACS Appl. Mater. Interfaces*, 2017, **9**, 3455–3462.

45 H. Zhang, Y.-H. Li, Y. Chen, M.-M. Wang, X.-S. Wang and X.-B. Yin, *Sci. Rep.*, 2017, **7**, 44153.

46 U. Ryu, H. S. Lee, K. S. Park and K. M. Choi, *Polyhedron*, 2018, **154**, 275–294.

47 J. Aguilera-Sigalat and D. Bradshaw, *Coord. Chem. Rev.*, 2016, **307**, 267–291.

48 K. Lu, T. Aung, N. Guo, R. Weichselbaum and W. Lin, *Adv. Mater.*, 2018, **30**, 1707634.

49 H. An, M. Li, J. Gao, Z. Zhang, S. Ma and Y. Chen, *Coord. Chem. Rev.*, 2019, **384**, 90–106.

50 S. Zhang, X. Pei, H. Gao, S. Chen and J. Wang, *Chin. Chem. Lett.*, 2020, **31**, 1060–1070.

51 S. Keskin and S. Kızılel, *Ind. Eng. Chem. Res.*, 2011, **50**, 1799–1812.

52 R. Liu, T. Yu, Z. Shi and Z. Wang, *Int. J. Nanomed.*, 2016, **11**, 1187–1200.

53 S. E. Miller, M. H. Teplensky, P. Z. Moghadam and D. Fairen-Jimenez, *Interface Focus*, 2016, **6**, 20160027.

54 J. Zhou, G. Tian, L. Zeng, X. Song and X. W. Bian, *Adv. Healthcare Mater.*, 2018, **7**, 1800022.

55 J. Yang and Y.-W. Yang, *View*, 2020, **1**, e20.

56 W. Sun, S. Li, G. Tang, Y. Luo, S. Ma, S. Sun, J. Ren, Y. Gong and C. Xie, *Int. J. Nanomed.*, 2019, **14**, 10195–10207.

57 S. M. Erturk, C. Johnston, C. Tempany-Afdhal and A. D. Van den Abbeele, in *Clinical and Translational Science*, ed. D. Robertson and G. H. Williams, Academic Press, San Diego, 2009, pp. 87–104.

58 P. Padmanabhan, A. Kumar, S. Kumar, R. K. Chaudhary and B. Gulyás, *Acta Biomater.*, 2016, **41**, 1–16.

59 K. M. Taylor-Pashow, J. Della Rocca, Z. Xie, S. Tran and W. Lin, *J. Am. Chem. Soc.*, 2009, **131**, 14261–14263.

60 S. Wuttke, S. Braig, T. Preiß, A. Zimpel, J. Sicklinger, C. Bellomo, J. O. Rädler, A. M. Vollmar and T. Bein, *Chem. Commun.*, 2015, **51**, 15752–15755.

61 F. Duan, X. Feng, X. Yang, W. Sun, Y. Jin, H. Liu, K. Ge, Z. Li and J. Zhang, *Biomaterials*, 2017, **122**, 23–33.

62 X. Liu, W. Qi, Y. Wang, R. Su and Z. He, *Nanoscale*, 2017, **9**, 17561–17570.

63 S. S. Nadar and V. K. Rathod, *Int. J. Biol. Macromol.*, 2017, **95**, 511–519.

64 C. Orellana-Tavra, S. Haddad, R. J. Marshall, I. Abánades Lázaro, G. Boix, I. Imaz, D. Maspoch, R. S. Forgan and D. Fairen-Jimenez, *ACS Appl. Mater. Interfaces*, 2017, **9**, 35516–35525.

65 J. Zielonka, J. Joseph, A. Sikora, M. Hardy, O. Ouari, J. Vasquez-Vivar, G. Cheng, M. Lopez and B. Kalyanaraman, *Chem. Rev.*, 2017, **117**, 10043–10120.

66 Y.-A. Li, X.-D. Zhao, H.-P. Yin, G.-J. Chen, S. Yang and Y.-B. Dong, *Chem. Commun.*, 2016, **52**, 14113–14116.

67 W. Zhou, L. Wang, F. Li, W. Zhang, W. Huang, F. Huo and H. Xu, *Adv. Funct. Mater.*, 2017, **27**, 1605465.

68 Y. Song, J. Yang, L. Wang and Z. Xie, *ChemMedChem*, 2020, **15**, 416–419.

69 S. Haddad, I. Abánades Lázaro, M. Fantham, A. Mishra, J. Silvestre-Albero, J. W. Osterrieth, G. S. Kaminski Schierle, C. F. Kaminski, R. S. Forgan and D. Fairen-Jimenez, *J. Am. Chem. Soc.*, 2020, **142**, 6661–6674.

70 U. P. Singh, N. Singh, R. Varshney, P. Roy and R. J. Butcher, *Cryst. Growth Des.*, 2018, **18**, 2804–2813.

71 W. Liu, Y. M. Wang, Y. H. Li, S. J. Cai, X. B. Yin, X. W. He and Y. K. Zhang, *Small*, 2017, **13**, 1603459.

72 H. Chen, J. Wang, D. Shan, J. Chen, S. Zhang and X. Lu, *Anal. Chem.*, 2018, **90**, 7056–7063.

73 D. F. Sava Gallis, L. E. Rohwer, M. A. Rodriguez, M. C. Barnhart-Dailey, K. S. Butler, T. S. Luk, J. A. Timlin and K. W. Chapman, *ACS Appl. Mater. Interfaces*, 2017, **9**, 22268–22277.

74 Y. Lv, D. Ding, Y. Zhuang, Y. Feng, J. Shi, H. Zhang, T.-L. Zhou, H. Chen and R.-J. Xie, *ACS Appl. Mater. Interfaces*, 2018, **11**, 1907–1916.

75 H. Zhao, G. Shu, J. Zhu, Y. Fu, Z. Gu and D. Yang, *Biomaterials*, 2019, **217**, 119332.

76 A. R. Chowdhuri, D. Laha, S. Pal, P. Karmakar and S. K. Sahu, *Dalton Trans.*, 2016, **45**, 18120–18132.

77 A. R. Chowdhuri, D. Laha, S. Chandra, P. Karmakar and S. K. Sahu, *Chem. Eng. J.*, 2017, **319**, 200–211.

78 Z. Yuan, L. Zhang, S. Li, W. Zhang, M. Lu, Y. Pan, X. Xie, L. Huang and W. Huang, *J. Am. Chem. Soc.*, 2018, **140**, 15507–15515.

79 L. He, T. Wang, J. An, X. Li, L. Zhang, L. Li, G. Li, X. Wu, Z. Su and C. Wang, *CrystEngComm*, 2014, **16**, 3259–3263.

80 J. Y. Zeng, M. K. Zhang, M. Y. Peng, D. Gong and X. Z. Zhang, *Adv. Funct. Mater.*, 2018, **28**, 1705451.

81 J. Deng, K. Wang, M. Wang, P. Yu and L. Mao, *J. Am. Chem. Soc.*, 2017, **139**, 5877–5882.

82 C. Orellana-Tavra, R. J. Marshall, E. F. Baxter, I. A. Lázaro, A. Tao, A. K. Cheetham, R. S. Forgan and D. Fairen-Jimenez, *J. Mater. Chem. B*, 2016, **4**, 7697–7707.

83 C. Orellana-Tavra, E. F. Baxter, T. Tian, T. D. Bennett, N. K. Slater, A. K. Cheetham and D. Fairen-Jimenez, *Chem. Commun.*, 2015, **51**, 13878–13881.

84 I. Abánades Lázaro, S. Haddad, S. Sacca, C. Orellana-Tavra, D. Fairen-Jimenez and R. S. Forgan, *Chem*, 2017, **2**, 561–578.

85 M. Javadi, W. G. Pitt, C. M. Tracy, J. R. Barrow, B. M. Willardson, J. M. Hartley and N. H. Tsosie, *J. Controlled Release*, 2013, **167**, 92–100.

86 H. Cai, Y.-L. Huang and D. Li, *Coord. Chem. Rev.*, 2019, **378**, 207–221.

87 J. Chen, Y. Zhu and S. Kaskel, *Angew. Chem., Int. Ed.*, 2021, **60**, 5010–5035.

88 S. Huh, S.-J. Kim and Y. Kim, *CrystEngComm*, 2016, **18**, 345–368.

89 C. Zou and C.-D. Wu, *Dalton Trans.*, 2012, **41**, 3879–3888.

90 J. Wang, Y. Fan, Y. Tan, X. Zhao, Y. Zhang, C. Cheng and M. Yang, *ACS Appl. Mater. Interfaces*, 2018, **10**, 36615–36621.

91 J. Liu, L. Zhang, J. Lei, H. Shen and H. Ju, *ACS Appl. Mater. Interfaces*, 2017, **9**, 2150–2158.

92 S. Lee, M. Baek, H.-Y. Kim, J.-H. Ha and D.-I. Jeoung, *Biotechnol. Lett.*, 2002, **24**, 1147–1151.

93 H. Mizutani, S. Tada-Oikawa, Y. Hiraku, M. Kojima and S. Kawanishi, *Life Sci.*, 2005, **76**, 1439–1453.

94 Y. C. Barenholz, *J. Controlled Release*, 2012, **160**, 117–134.

95 F. D. Duman, M. Erkisa, R. Khodadust, F. Ari, E. Ulukaya and H. Y. Acar, *Nanomedicine*, 2017, **12**, 2319–2333.

96 J. Prados, C. Melguizo, R. Ortiz, C. Velez, P. J. Alvarez, J. L. Arias, M. A. Ruiz, V. Gallardo and A. Aranega, *Anti-Cancer Agents Med. Chem.*, 2012, **12**, 1058–1070.

97 J.-C. G. Bünzli and C. Piguet, *Chem. Soc. Rev.*, 2005, **34**, 1048–1077.

98 M. A. Alcala, C. M. Shade, H. Uh, S. Y. Kwan, M. Bischof, Z. P. Thompson, K. A. Gogick, A. R. Meier, T. G. Strein and D. L. Bartlett, *Biomaterials*, 2011, **32**, 9343–9352.

99 P. Nockemann, E. Beurer, K. Driesen, R. Van Deun, K. Van Hecke, L. Van Meervelt and K. Binnemans, *Chem. Commun.*, 2005, 4354–4356.

100 S. Weissman, *J. Chem. Phys.*, 1942, **10**, 214–217.

101 J. Wang, W. Sun, S. Chang, H. Liu, G. Zhang, Y. Wang and Z. Liu, *RSC Adv.*, 2015, **5**, 48574–48579.

102 D. Hu, Y. Song and L. Wang, *J. Nanopart. Res.*, 2015, **17**, 310.

103 R. Abazari, F. Ataei, A. Morsali, A. M. Slawin and C. L. Carpenter-Warren, *ACS Appl. Mater. Interfaces*, 2019, **11**, 45442–45454.

104 A. M. Smith, M. C. Mancini and S. Nie, *Nat. Nanotechnol.*, 2009, **4**, 710–711.

105 D. Wang, C. Zhao, G. Gao, L. Xu, G. Wang and P. Zhu, *Nanomaterials*, 2019, **9**, 1274.

106 Y. Zhuang, Y. Katayama, J. Ueda and S. Tanabe, *Opt. Mater.*, 2014, **36**, 1907–1912.

107 J. W. Chung, Z. Gerelkhuu, J. H. Oh and Y.-I. Lee, *Appl. Spectrosc. Rev.*, 2016, **51**, 678–705.

108 F. D. Duman, I. Hocaoglu, D. G. Ozturk, D. Gozuacik, A. Kiraz and H. Y. Acar, *Nanoscale*, 2015, **7**, 11352–11362.

109 I. Hocaoglu, F. Demir, O. Birer, A. Kiraz, C. Sevrin, C. Grandfils and H. Y. Acar, *Nanoscale*, 2014, **6**, 11921–11931.

110 X. Lin, G. Gao, L. Zheng, Y. Chi and G. Chen, *Anal. Chem.*, 2014, **86**, 1223–1228.

111 D. Zhao, X. Wan, H. Song, L. Hao, Y. Su and Y. Lv, *Sens. Actuators, B*, 2014, **197**, 50–57.

112 H. Zhao, C. Serre, E. Dumas and N. Steunou, in *Metal-Organic Frameworks for Biomedical Applications*, ed. M. Mosafari, Elsevier, 2020, pp. 397–423.

113 J. Jiang, H. Gu, H. Shao, E. Devlin, G. C. Papaefthymiou and J. Y. Ying, *Adv. Mater.*, 2008, **20**, 4403–4407.

114 X. Wang, P. Li, Q. Ding, C. Wu, W. Zhang and B. Tang, *J. Am. Chem. Soc.*, 2019, **141**, 2061–2068.

115 C. Yang, X. Yin, S.-Y. Huan, L. Chen, X.-X. Hu, M.-Y. Xiong, K. Chen and X.-B. Zhang, *Anal. Chem.*, 2018, **90**, 3118–3123.

116 S. W. Botchway, M. Charnley, J. W. Haycock, A. W. Parker, D. L. Rochester, J. A. Weinstein and J. G. Williams, *Proc. Natl. Acad. Sci. U. S. A.*, 2008, **105**, 16071–16076.

117 W. A. Maza, R. Padilla and A. J. Morris, *J. Am. Chem. Soc.*, 2015, **137**, 8161–8168.

118 W. A. Maza and A. J. Morris, *J. Phys. Chem. C*, 2014, **118**, 8803–8817.

119 R. Chen, J. Zhang, J. Chelora, Y. Xiong, S. V. Kershaw, K. F. Li, P.-K. Lo, K. W. Cheah, A. L. Rogach and J. A. Zapien, *ACS Appl. Mater. Interfaces*, 2017, **9**, 5699–5708.

120 C. Yang, K. Chen, M. Chen, X. Hu, S.-Y. Huan, L. Chen, G. Song and X.-B. Zhang, *Anal. Chem.*, 2019, **91**, 2727–2733.

121 X. Mao, J. Xu and H. Cui, *Wiley Interdiscip. Rev.: Nanomed. Nanobiotechnol.*, 2016, **8**, 814–841.

122 M. Peller, K. Böll, A. Zimpel and S. Wuttke, *Inorg. Chem. Front.*, 2018, **5**, 1760–1779.

123 W. Zhang, L. Liu, H. Chen, K. Hu, I. Delahunty, S. Gao and J. Xie, *Theranostics*, 2018, **8**, 2521–2548.

124 J. Estelrich, M. J. Sánchez-Martín and M. A. Busquets, *Int. J. Nanomed.*, 2015, **10**, 1727–1741.

125 W. Lin, T. Hyeon, G. M. Lanza, M. Zhang and T. J. Meade, *MRS Bull.*, 2009, **34**, 441–448.

126 A. Pandey, N. Dhas, P. Deshmukh, C. Caro, P. Patil, M. L. García-Martín, B. Padya, A. Nikam, T. Mehta and S. Mutalik, *Coord. Chem. Rev.*, 2020, **409**, 213212.

127 M. Rogosnitzky and S. Branch, *Biometals*, 2016, **29**, 365–376.

128 C. Olchowy, K. Cebulski, M. Łasecki, R. Chaber, A. Olchowy, K. Kałwak and U. Zaleska-Dorobisz, *PLoS One*, 2017, **12**, e0171704.

129 P. Caravan, J. J. Ellison, T. J. McMurry and R. B. Lauffer, *Chem. Rev.*, 1999, **99**, 2293–2352.

130 Z. Zhou and Z. R. Lu, *Wiley Interdiscip. Rev.: Nanomed. Nanobiotechnol.*, 2013, **5**, 1–18.

131 J. Ramalho and M. Ramalho, *Magn. Reson. Imaging Clin. N. Am.*, 2017, **25**, 765–778.

132 H. S. Thomsen, P. Marckmann and V. B. Logager, *Cancer Imaging*, 2007, **7**, 130–137.

133 R. C. Semelka, J. P. Prybylski and M. Ramalho, *Magn. Reson. Imaging*, 2019, **58**, 174–178.

134 L. Pasquini, A. Napolitano, E. Visconti, D. Longo, A. Romano, P. Tomà and M. C. R. Espagnet, *CNS Drugs*, 2018, **32**, 229–240.

135 M. A. Chowdhury, *J. Biomed. Mater. Res., Part A*, 2017, **105**, 1184–1194.

136 H.-X. Zhao, Q. Zou, S.-K. Sun, C. Yu, X. Zhang, R.-J. Li and Y.-Y. Fu, *Chem. Sci.*, 2016, **7**, 5294–5301.

137 D. Wang, J. Zhou, R. Chen, R. Shi, G. Zhao, G. Xia, R. Li, Z. Liu, J. Tian and H. Wang, *Biomaterials*, 2016, **100**, 27–40.

138 D. Wang, J. Zhou, R. Chen, R. Shi, G. Xia, S. Zhou, Z. Liu, N. Zhang, H. Wang and Z. Guo, *Biomaterials*, 2016, **107**, 88–101.

139 D. Pan, A. H. Schmieder, S. A. Wickline and G. M. Lanza, *Tetrahedron*, 2011, **67**, 8431–8444.

140 J. Della Rocca and W. Lin, *Eur. J. Inorg. Chem.*, 2010, 3725–3734.

141 Y. Yang, J. Liu, C. Liang, L. Feng, T. Fu, Z. Dong, Y. Chao, Y. Li, G. Lu and M. Chen, *ACS Nano*, 2016, **10**, 2774–2781.

142 L. Qin, Z.-Y. Sun, K. Cheng, S.-W. Liu, J.-X. Pang, L.-M. Xia, W.-H. Chen, Z. Cheng and J.-X. Chen, *ACS Appl. Mater. Interfaces*, 2017, **9**, 41378–41386.

143 N. Lee and T. Hyeon, *Chem. Soc. Rev.*, 2012, **41**, 2575–2589.

144 F. Shu, D. Lv, X.-L. Song, B. Huang, C. Wang, Y. Yu and S.-C. Zhao, *RSC Adv.*, 2018, **8**, 6581–6589.

145 A. R. Chowdhuri, D. Bhattacharya and S. K. Sahu, *Dalton Trans.*, 2016, **45**, 2963–2973.

146 H.-S. Wang, *Coord. Chem. Rev.*, 2017, **349**, 139–155.

147 F. A. Mettler Jr, P. W. Wiest, J. A. Locken and C. A. Kelsey, *J. Radiol. Prot.*, 2000, **20**, 353–359.

148 A. M. Leung and L. E. Braverman, *Curr. Opin. Endocrinol., Diabetes Obes.*, 2012, **19**, 414–419.

149 M. Andreucci, R. Solomon and A. Tasanarong, *BioMed Res. Int.*, 2014, **2014**, 872574.

150 C. Wang, O. Volotskova, K. Lu, M. Ahmad, C. Sun, L. Xing and W. Lin, *J. Am. Chem. Soc.*, 2014, **136**, 6171–6174.

151 S. Basu and A. Alavi, *PET Clinics*, 2016, **11**, 203–207.

152 O. Jacobson and X. Chen, *Pharmacol. Rev.*, 2013, **65**, 1214–1256.

153 M. Hamoudeh, M. A. Kamleh, R. Diab and H. Fessi, *Adv. Drug Delivery Rev.*, 2008, **60**, 1329–1346.

154 D. Duan, H. Liu, M. Xu, M. Chen, Y. Han, Y. Shi and Z. Liu, *ACS Appl. Mater. Interfaces*, 2018, **10**, 42165–42174.

155 S. Zackrisson, S. Van De Ven and S. Gambhir, *Cancer Res.*, 2014, **74**, 979–1004.

156 H. F. Zhang, K. Maslov, G. Stoica and L. V. Wang, *Nat. Biotechnol.*, 2006, **24**, 848–851.

157 R. G. Kolkman, P. J. Brands, W. Steenbergen and T. G. van Leeuwen, *J. Biomed. Opt.*, 2008, **13**, 050510.

158 J. Zhang, H. Chen, T. Zhou, L. Wang, D. Gao, X. Zhang, Y. Liu, C. Wu and Z. Yuan, *Nano Res.*, 2017, **10**, 64–76.

159 Y. Yang, Y. Chao, J. Liu, Z. Dong, W. He, R. Zhang, K. Yang, M. Chen and Z. Liu, *NPG Asia Mater.*, 2017, **9**, e344.

160 D. Zhang, H. Xu, X. Zhang, Y. Liu, M. Wu, J. Li, H. Yang, G. Liu, X. Liu and J. Liu, *ACS Appl. Mater. Interfaces*, 2018, **10**, 25203–25212.

161 W. Cai, J. Wang, H. Liu, W. Chen, J. Wang, L. Du, J. Hu and C. Wu, *J. Alloys Compd.*, 2018, **748**, 193–198.

162 T. Kundu, S. Mitra, D. D. Díaz and R. Banerjee, *ChemPlusChem*, 2016, **81**, 728–732.

163 X. Gao, G. Ji, R. Cui, J. Liu and Z. Liu, *Dalton Trans.*, 2017, **46**, 13686–13689.

164 Y. Li, J. Tang, L. He, Y. Liu, Y. Liu, C. Chen and Z. Tang, *Adv. Mater.*, 2015, **27**, 4075–4080.

165 C. Tian, L. Zhu, F. Lin and S. G. Boyes, *ACS Appl. Mater. Interfaces*, 2015, **7**, 17765–17775.

166 X. Chen, M. Zhang, S. Li, L. Li, L. Zhang, T. Wang, M. Yu, Z. Mou and C. Wang, *J. Mater. Chem. B*, 2017, **5**, 1772–1778.

167 X. Song, C. Liang, H. Gong, Q. Chen, C. Wang and Z. Liu, *Small*, 2015, **11**, 3932–3941.

168 X. Liang, Y. Li, X. Li, L. Jing, Z. Deng, X. Yue, C. Li and Z. Dai, *Adv. Funct. Mater.*, 2015, **25**, 1451–1462.

169 K. Yang, H. Xu, L. Cheng, C. Sun, J. Wang and Z. Liu, *Adv. Mater.*, 2012, **24**, 5586–5592.

170 Z. Zha, Z. Deng, Y. Li, C. Li, J. Wang, S. Wang, E. Qu and Z. Dai, *Nanoscale*, 2013, **5**, 4462–4467.

171 P. Yang, Y. Men, Y. Tian, Y. Cao, L. Zhang, X. Yao and W. Yang, *ACS Appl. Mater. Interfaces*, 2019, **11**, 11209–11219.

172 W. Shang, C. Zeng, Y. Du, H. Hui, X. Liang, C. Chi, K. Wang, Z. Wang and J. Tian, *Adv. Mater.*, 2017, **29**, 1604381.

173 Y. Liu, Y. Zhao and X. Chen, *Theranostics*, 2019, **9**, 3122–3133.